Direct numerical simulation of dispersion and mixing in gas-liquid Dean-Taylor flow with influence of a 90° bend

O. Mierka, R. Münster, J. Surkamp, S. Turek, N. Kockmann

Direct numerical simulation of dispersion and mixing in gas-liquid Dean-Taylor flow with influence of a 90° bend

Otto Mierka[a,*], Raphael Münster[a], Julia Surkamp[b], Stefan Turek[a], Norbert Kockmann[b,*]

[a]Department of Mathematics, Institute for Applied Mathematics (LS3), TU Dortmund University, Vogelpothsweg 87, 44227 Dortmund, Germany
[b]Department of Biochemical and Chemical Engineering, Laboratory of Equipment Design, TU Dortmund University, Emil-Figge-Strasse 68, 44227 Dortmund, Germany
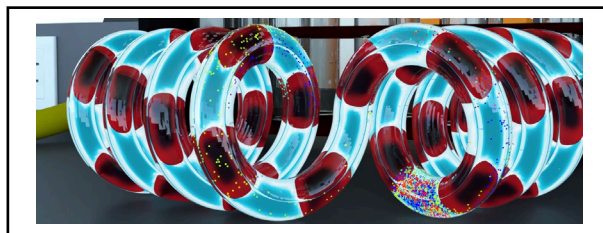* Correspondence: omierka@mathematik.tu-dortmund.de, norbert.kockmann@tu-dortmund.de

KEYWORDS: gas-liquid capillary flow; Dean flow; Taylor flow; direct numerical simulation; finite element method; particle dispersion measurement

HIGHLIGHTS:

- *Direct numerical simulation of full 3D flow fields*
- *Particle dispersion to evaluate flow mixing effects*
- *Influence of flow velocity in comparison of the coil diameter*
- *Coupled Dean and Taylor flow with 90° bend influence*

GRAPHICAL ABSTRACT

Supporting information:

https://doi.org/10.17877/tudodata-2024-lwoxtgmw

for review:

https://data.tu-dortmund.de/privateurl.xhtml?token=129143c4-0373-4e68-b446-80e613b9b0b5

ABSTRACT

Gas-liquid capillary flow finds widespread applications in reaction engineering, owing to its ability to facilitate precise control and efficient mixing. Incorporating compact and regular design with Coiled Flow Inverter (CFI) enhances process efficiency due to improved mixing as well as heat and mass transfer leading to a narrow residence time distribution. The impact of Dean and Taylor flow phenomena on mixing and dispersion within these systems underscores their significance, but is still not yet fully understood. Direct numerical simulation based on finite element method enables full 3D resolution of the flow field and detailed examination of laminar flow profiles, providing valuable insights into flow dynamics. Notably, the deflection of flow velocity from the center axis contributes is followed by tracking of particle with defined starting positions, aiding in flow visualization and dispersion characterization. In this CFD study, the helical flow with the influence of the centrifugal force and pitch (Dean flow) as well as the capillary two-phase flow (Taylor bubble) is described and characterized by particle dispersion and related histograms. Future prospects in this field include advancements in imaging techniques to capture intricate flow patterns, as well as refined particle tracking methods to better understand complex flow behavior.

1. Introduction

Microstructured and capillary reactors have been used for many years to carry out chemical and biochemical reactions on a very small scale, see Kockmann (2006) or Hessel et al. (2015). The small volumes reduce the cost of materials and energy. This reduces the handling of hazardous materials and promotes the protection of people and the environment (Srinivasan and Natarajan (2012) or Kockmann et al. (2011)). A large surface-to-volume ratio simplifies temperature control, counteracting, for example, thermal runaway starting from exothermic reaction, see Kashid et al. (2011). The improved mass and heat transfer properties in micro-process engineering make the application of microreactors in research and industry particularly interesting, see Zhang et al. (2004) for process development or López-Guajardo et al. (2017) for multiphase reactions, and forms a base for intensified, optimized, and environmentally friendly processes (Bolivar and Nidetzky (2013)) for biocatalytic processes in flow.

Process intensification and process control belong to the main objectives of chemical engineering, which are only then approachable if the understanding of all relevant processes is available or accessible. Aside of experimental analysis CFD methods are well accepted frameworks serving for these purposes in a wide range of chemical engineering applications. However, in the field of multi-physics processes only those CFD techniques might contribute with reliable prediction possibilities which are equipped with the combination of suitable discretization methods and efficient numerical approaches. Typical example of such type of problems is related to Taylor bubble flows in curved capillaries, which is subject to multiphase flows with dynamically evolving interfaces and the presence of thin laminar film layers between the dispersed phase and the capillary wall. Pioneering works in this regard reach back to a steady, spatially periodical simulation framework presented by Kashid et al. (2007a). A remarkable review of CFD methods used for individual Taylor bubble flows in more complex geometries have been provided by Wörner (2012). Axisymmetric simulations of straight capillaries with transport of species and chemical reactions have been provided by Yang et al. (2017). The recent work of Chatterjee et al. (2021) demonstrated the formation (pinch off) of the bubbles and their respective transportation in straight and curved capillaries under wetting conditions by the use of contact angle boundary conditions at the triple phase contact lines.

The most accurate simulation approach so far presented in the framework of Taylor bubble flows within curved capillaries has been so far presented by Gaddem et al. (2021), who have utilized a suitable transformation method making it possible to resolve the bubble transportation under non-wetting conditions. Moreover, the transport of species and performance of chemical reactions have also been analyzed based on the computationally determined flow fields. Numerical simulation of Taylor flows in CFI geometries involves the simulation of multiphase flows with dynamically resolved interfaces in curved capillaries. The primary challenge hindering the computational realization of these flows is the dynamically changing interface within a confined round capillary, leading to the formation of thin films whose resolution

may impose extreme stability limits on the underlying simulation tool. Strictly speaking, numerical frameworks that do not support a sharp resolution of the interface render most multiphase simulation software inapplicable, unless used with significant computational overhead to allow for the precise resolution of the liquid film between gas bubbles and liquid slugs. Pioneering works in this regard focus on the simulation of Taylor bubbles in straight capillaries:

- Lizarraga-Garcia et al. (2017, 2021) utilized a Level Set method combined with the Immersed Surfaces Technique, implemented into the Finite Volume simulation software TransAT,

- Gutiérrez et al. (2017) employed a 3D Volume-of-Fluid (VOF) method,

- Massoud et al. (2018) utilized a 2D (axisymmetric) Conservative Level Set method with a moving mesh technique,

- Abubakar and Matar (2021) employed a 2D (axisymmetric) Elastic Mesh Update Method within a Finite Element Method (FEM) framework, discretized with higher order quadratic elements for both the flow field variables and the deformation equation.

These works collectively cover a wide range of Eötvös and Morton numbers, which characterize the underlying simulation setups. Moreover, they also address full 3D cases of non-axisymmetric setups such as tilted capillaries. Advanced simulation works extend to the simulation of Taylor bubble dynamics within annular capillaries, as demonstrated by Liu et al., (2023) using the VOF method in ANSYS. A common feature among all these works is the condition where the fluid surrounding the bubble remains stagnant, with its rise being driven by buoyant effects. Under forced conditions, such as considering an effective flow rate through the capillary, bubble dynamics result in the formation of narrow films between the bubble and the capillary wall. It is noteworthy that numerical studies dealing with more than 2-3 Taylor bubbles are exceedingly rare, with few exceptions such as the work by Araújo et al., (2013), or are not available at all, particularly concerning the simulation of a row of Taylor bubbles in curved-like capillaries.

Simulation attempts focusing on fully resolved (with interface aligned meshes) Taylor bubble flows in a large geometrical representation of CFIs have not been described so far and, therefore, are the central focus of this work. The numerical framework has already been defined in the computational framework of single Taylor bubbles in Mierka and Turek (2021), which in the current work has been extended towards multiple bubbles in arbitrarily curved capillaries. The simulation framework employed in this work represents a further development of the basic concept implemented into the open-source software package FeatFlow. This framework is based on a front tracking, Finite Element Method (FEM) discretized mesh deformation method governed by the linear elasticity model. Discretization is performed using the higher order iso-parametric $Q_2/P_1/Q_2$ (velocity, pressure, displacement) elements to allow for the representation of element-wise curved interfaces. The underlying method benefits from accurately representing interfacial tension forces as semi-implicitly treated surface integrals within the framework of the Laplace-Beltrami transformation.

This method has already demonstrated its potential in benchmark computations such as the 3D rising bubble, providing reference results with unprecedented precision (see Turek et al., (2019)). Additionally, it has facilitated the first real convergence analysis and reference results for the Taylor bubble benchmark of Marschall et al., (2014), as demonstrated by Mierka and Turek (2021).

The use of a two-phase mixture leads to axial dispersion and thus to better mixing and improved mass transfer (Bolivar and Nidetzky, 2013). A periodic succession of two phases in a capillary results in the formation of internal Taylor vortices, which overcome mass transport limitations due to good mixing (Taylor, 1961; Gelhausen et al., 2014). Secondary vortices form in a curved capillary. The superposition of the two vortices leads to pronounced radial mixing (Rojahn et al., 2018; Sudarsan and Ugaz, 2006; Kumar et al., 2006). The additional 90° deflections in a coiled flow inverter (CFI) intensify these effects (Klutz et al., 2015). This results in further mass transfer enhancements and a narrow residence time distribution (Vashtish and Nigam, 2008).

Essential reactions in chemistry as well as in biochemistry are gas-liquid reactions such as oxidation, hydrogenation or carboxylation. Here mass transfer is often limiting, which is why these are often applied in capillary reactors to benefit from the high specific surface area and mass transfer (Hessel et al., 2005). Developing a process with a very specific reaction is challenging, but this can enable a very high potential for industry (Kashid et al., 2007b) with heat transfer limited liquid-liquid reactions. The CFI allows a fast analysis at different process and reaction conditions (Bobers et al., 2020). This contribution shows the mixing and dispersion conditions in a gas-liquid flow CFI and how this setup can be used for process development (Grühn et al., 2022).

The here presented work is dedicated to the development of a software analysis tool specialized for Taylor bubble flows in a wide range of applications and covering a variety of geometrical realizations. After the overview about the current status of periodic gas-liquid flow in helical capillaries, a higher order FEM based interface tracking (IT) simulation software is presented, which due to the underlying isoparametric discretization and interface aligned mesh construction allows a semi-implicit treatment of the surface tension force term. This framework guarantees a negligible mass loss rate resulting in a suitable tool for long time-scale simulations. Exploiting these numerical advantages, the software has been applied for the system of Coiled Flow Inverter (CFI) capillaries with three representative coil diameters and three different Reynolds numbers. The pseudo-periodic flow field was investigated for further mixing quantification studies by the help of particle tracking based analysis. In the framework of this postprocessing analysis such a suitable transformation of the results was found, which reveals the most important features of the characteristic flow patterns. Further, the analysis was able not only qualitatively but even quantitatively to characterize the behavior of the established flow patterns.

2. Status of Periodic Gas-liquid Capillary Flow

The following explains the fundamentals of dimensionless numbers, different gas-liquid flow patterns, and the Taylor bubble flow in straight and curved capillaries.

2.1. Dimensionless numbers

For typical liquid single phase and gas-liquid two phase flows, dimensionless numbers are used to describe typical flow phenomena and flow regimes due to the relation of relevant forces, length scales, or time relations. The most important relation in flow fields is the ratio of momentum to viscous force, expressed in the Reynolds number Re

$$\mathrm{Re} = \frac{\rho \, v \, d_h}{\mu} = \frac{v \, d_h}{\nu} \tag{1}$$

with the fluid density ρ, the flow velocity v, the dynamic and kinematic viscosity μ and ν, respectively, and the hydraulic diameter d_h, which is defined as ratio of 4-times the cross section divided by the wetted perimeter. For low flow velocities and small diameters, laminar flow predominates (Day et al., (2012)), in particular for capillary flow with Re numbers often below 10. In these length scales, the surface tension with Laplace pressure gains importance, which is expressed by the force ratio of viscous force to the surface tension σ, the Capillary number

$$\mathrm{Ca} = \frac{\mu \, v}{\sigma} \tag{2}$$

where the viscosity of continuous phase is usually used. The product of the Reynolds and Capillary number is the so-called Weber number, relating momentum force with surface tension

$$\mathrm{We} = \mathrm{Re} \cdot \mathrm{Ca} = \frac{\rho \, v^2 \, d_h}{\sigma} \tag{3}$$

This number is important for droplet or bubble generation processes as well as for two-phase flow regimes. To estimate the influence of gravitational acceleration g, the Bond number Bo relates the gravitational force from a density difference $\Delta\delta$ to the surface tension

$$\mathrm{Bo} = \frac{\Delta\delta \, g \, L^2}{\sigma} \tag{4}$$

Since the CFI consists of a helical capillary, the dominant forces are supplemented by the centrifugal force acting on the flowing fluids, in particular on the heavier liquid phases. The Dean number Dn is formed to include the centrifugal force.

$$\mathrm{Dn} = \mathrm{Re} \sqrt{\frac{d_h}{d_c}} = \frac{v \, d_h}{\nu} \sqrt{\frac{d_h}{d_c}} \tag{5}$$

with the ratio of the hydraulic diameter to the coil diameter. Since this ratio is often smaller than 1, the Dn number is smaller than the Re number.

2.2. Flow patterns in gas-liquid capillary flow

Depending on the forces mentioned above and the droplet formation process, different flow forms appear in capillary gas-liquid flows (Waelchli and von Rohr (2006)). The channel geometry and the nature of the

6

channel surface influence the wetting characteristics and thus the formation of different regimes. Parameters such as temperature, which affects the surface tension of the fluids, also have a strong influence (Shao et al., (2009)) but are not considered here. Furthermore, the mechanism of bubble generation plays a role (Akbar et al., (2003)). In a capillary, the following regimes can be observed for gas-liquid flows (Sobieszuk et al., (2012)):

- Bubble flow for low gas flow rates,
- Taylor film flow with wetting continuous phase,
- Taylor box flow with non-wetting continuous phase,
- Churn flow for high gas and liquid flow rates,
- Ring flow for high gas flow rates.

The Taylor flow is characterized by a periodic sequence of gas bubbles and liquid slugs with stable and repeatable behavior. The gas bubbles have a greater length than the channel inner diameter (Kashid et al., 2011). This flow form divides into a Taylor box flow or Taylor film flow depending on the wetting properties. While in film flow, the bubbles are surrounded by a thin liquid film, this phenomenon does not occur in box flow. Here, the caps of the bubbles do not have a semicircular shape. Since there is a smaller contact area with the liquid in box flow, less mass transfer is the result (Taitel et al., 1980). Churn and ring flow are not treated in this contribution.

2.3. Taylor bubble flow in straight capillaries

Taylor film flow is particularly well suited for mass transfer studies due to the regular and stable flow patterns and high mass transfer rates. The reasons for this, besides the high surface-to-volume ratio, are the formation of internal vortices in both phases. These vortices were discovered by Geoffrey Taylor in 1961 and were thus named Taylor vortices (Gelhausen et al., 2014). Due to the Taylor vortices, there is a circulatory motion within the fluid slug (Dani et al., 2007; Stieglitz and Ehrhard, 2012), see Figure 1.
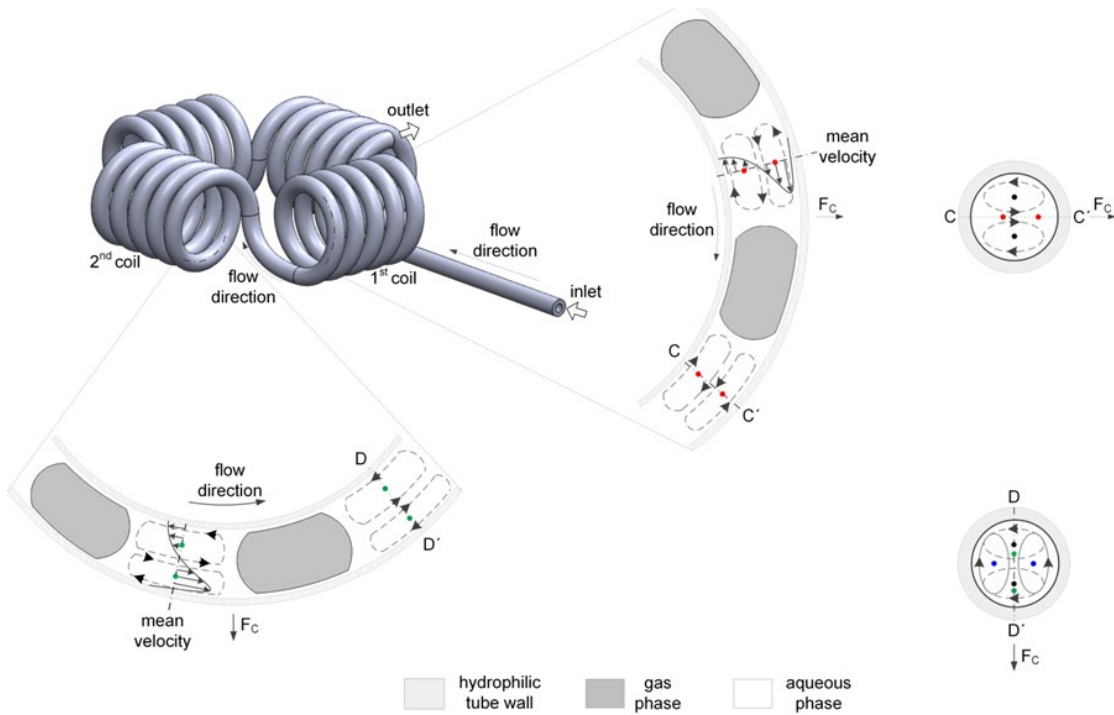

flow direction
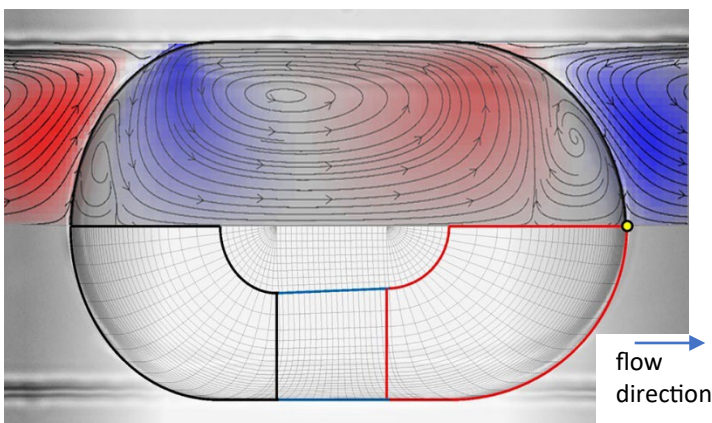
Figure 1: Single bubble flow in capillaries with symmetric streamlines and comparison of surface shape in simulation and experiment, adapted from Miessner et al., (2020).

The reason of the formation of these vortices is due to the parabolic velocity profile, caused by the static friction on the capillary wall and the deflection due to the gas-liquid interface. The fluid in the core is forced toward the wall as it progresses to the interface. The fluid at the wall continues to flow along the wall until it passes back to the core of the capillary and is accelerated. In the center of the formed vortex is the so-called stagnant ring. In this region, mass transport is limited by diffusion. Due to the Taylor vortices, continuous circulating mixing occurs, which is dominated by convection. Thus, despite a laminar flow, enhanced mass transfer is achieved.

2.4. Taylor bubble flow in curved capillaries

Secondary vortices are formed in curved capillaries due to the additional centrifugal force (Gelhausen et al., 2014). The resulting secondary vortices are called Dean vortices (Dean, 1928; Saxena and Nigam, 1984). Unlike in straight capillaries, there is no symmetrical velocity profile, but the fluid moves faster in the outer (top) region of the capillary than in the inner (bottom) region, see Figure 2. Thus, a fluid movement from the core flow to the outside of the bend is observed (Vashtish and Nigam, 2008; Kurt et al., 2017). The fundamental situation of combined Taylor and Dean flow is depicted in Figure 2, right part. The cross section in the axial plane along the tube direction shows the "double vortex" of the Taylor flow with slightly larger vortex area in the inner region, since the flow velocity in the outer region is accelerated by the centrifugal force (middle and lower left part in Figure 2). The cross section in the radial plane of C-C' shows the vortex pair of the Dean flow due to the centrifugal force with the two black points as centers of the vortices. The red points indicate the center lines of the Taylor vortices. After the 90° bend, cross section of D-D', the centrifugal force is deflected to 90°, too, which leads to the new orientation of the Dean vortices and the related center points (blue points). This is assumed to increase the internal mixing, which is discussed in more detail by Kurt et al. (2017) and will be further elaborated in this contribution.

Figure 2: Gas-liquid slug flow mixing behavior in a coiled flow inverter, adapted from Kurt et al. (2017).

The centrifugal force leads to an outward directed central flow as indicated by the Dean flow, disturbing the Taylor flow. This core flow deflection can be clearly seen by the deflection of the core flow in Figure 3.
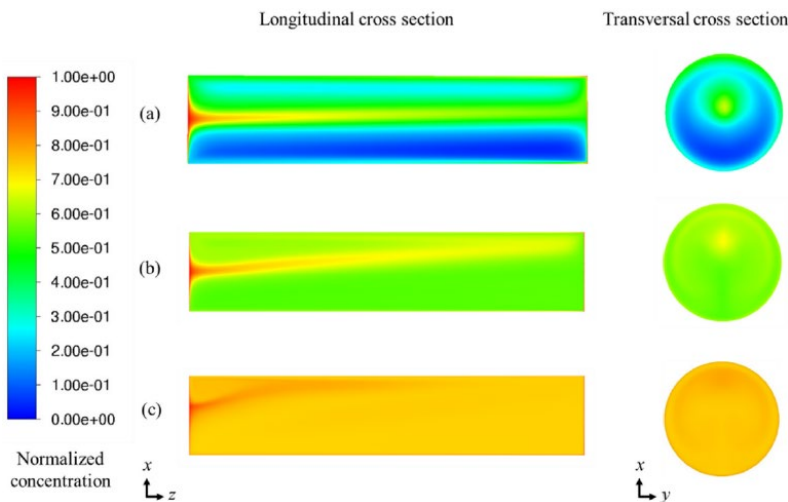
Figure 3: Concentration distribution of dissolved oxygen from convection and division in a plug flow droplet with a) $u = 0.01$ m s^{-1} (Dn = 2.2), b) $u = 0.05$ m s^{-1} (Dn = 11.2), and c) $u = 0.15$ m s^{-1} (Dn = 33.5), adapted from Gaddem et al. (2021).

The influence of centrifugal force gets stronger with increasing flow velocity. However, the numerical simulation in Figure 3 suffers from numerical diffusion and smearing of the concentration gradient. The deflection of the core flow due to centrifugal forces could also be observed in experimental studies of Krieger et al., 2017, and Schlüter et al., 2021, see Figure 4. With increasing flow velocity, the radial deflection of the core flow gets larger, until higher shear rates lead to more vortex generation disturbing the core flow, see Regime 3 in Figure 4.
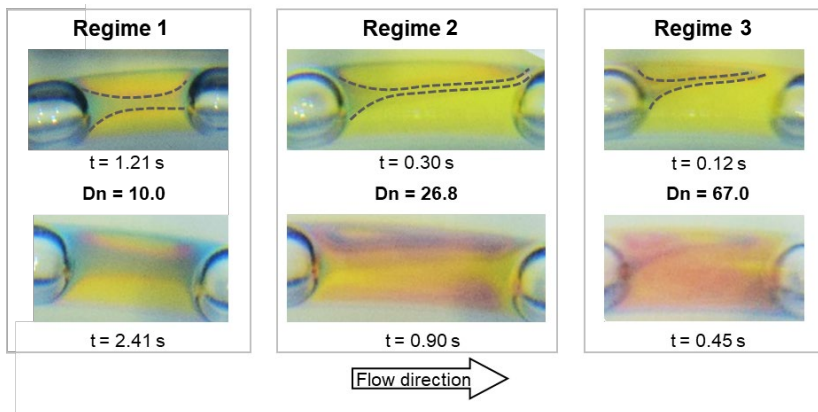
Figure 4: Images of slug flow in a coiled capillary with inner tube diameter of 1.6 mm and coil diameter of 38.2 mm depicting the oxidation of leuco-indigo carmine by synthetic air. Three different flow regimes are shown at two different time steps, adapted from Schlüter et al. (2021).

Similar flow behavior was observed by Müller et al. (2021) in an extensive experimental study of gas-liquid flow in a helical tube with inner diameter of 4 mm and a coil diameter of 42 mm. The investigated Re number ranges from 300 to nearly 1100, which often lead to irregular flow with disturbed secondary vortices. However, the deflected flow of the core was also in the entire range of Re numbers. The authors defined a mixing coefficient from the intensity difference from the measured location of tracer particles. The values of this coefficient varied in a wide range, however, the mean value was high for high gas velocities, but nearly independent from the liquid velocity.

Due to the superposition of the Dean and the Taylor vortices, a pronounced radial mixing occurs. This leads to a further enhancement of mass transfer (Roudet et al., 2011). A phenomenological explanation of these coupled phenomena given in Figure 2, however, numerical modeling suffered up to now from the complex nature of the full 3D problem.

3. Numerical Methods

This work marks the first instance of utilizing the underlying framework for the analysis of a sequence of several Taylor bubbles in combination with curved capillaries, referring to the CFI geometrical representation. The numerical simulation method is based on the open source Finite Element Method (FEM) software package FeatFlow (Turek, 1997), which has been extended with additional numerical techniques. This allows numerical simulations of geometrically non-trivial curved capillary systems with a two-phase Taylor bubble flow. The considered geometrical setups are shown in Figure 5.
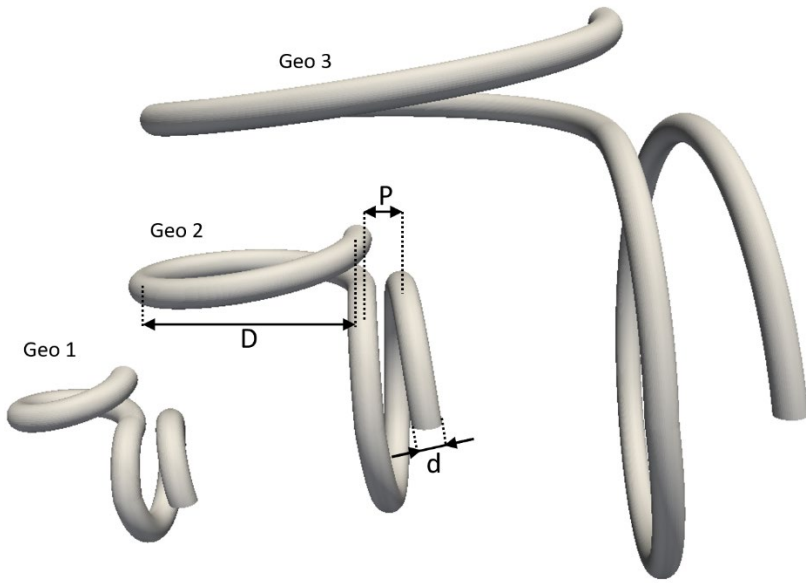
Figure 5: Visual representations of the 3 computationally considered geometrical CFI variants consisting of the inflow coil (2π), inverter bend ($\pi/4$) and outflow coil (2π).

The geometrical and operational details to Figure 5 are given in Table 1.

Table 1: Summary of the computationally considered cases. d – capillary diameter with 1.6 mm, D – coil diameter, P – pitch length of the coil, $\overline{v}$ – average velocity (flow rate divided by cross-sectional area). "Geo" stands for the geometrical variants (see Figure 5), "Op" stands for the respective operation condition (flow rate).

Entry	Geo1/Op1	Geo2/Op1	Geo2/Op2	Geo3/Op1	Geo3/Op2	Geo3/Op3
$D\,[mm]$	6.0	12.0	12.0	24.0	24.0	24.0
$P\,[mm]$	3.0	3.0	3.0	6.0	6.0	6.0
$\overline{v}\,[mm\,s^{-1}]$	30.0	30.0	60.0	30.0	60.0	120.0
$\sigma_{l/g}\,[N\cdot m^{-1}]^*$	0.0025	0.0050	0.0100	0.0050	0.0100	0.0200
Re g-l	42.9/3.2	42.9/3.2	85.7/6.4	42.9/3.2	85.7/6.4	171.4/12.8
Dn g-l	22.1/1.7	15.7/1.2	31.3/2.3	11.1/0.83	22.1/1.7	44.3/3.3

The Re and Dn numbers are calculated with the liquid and gas density of 1000 and 1.2 kg m^{-3} and viscosity of 0.00112 and 0.000015 Pa s, respectively. The Ca number ranges from 0.00672 to 0.02688, while the Bo number is 9.2 for all cases, indicating the low influence of surface tension compared to viscous or gravitation forces. The We number ranges from 0.288 to 4.608 and 0.0215 to 0.344 for the liquid and gas phase, respectively.

The main features of the utilized FeatFlow solver gather the techniques related to geometric multigrid methods based fast solvers, domain decomposition based MPI parallelization, and a higher order FEM discretization of the Navier-Stokes equations extended with isoparametric geometric approximation of curved boundaries. These are essentially the main numerical properties that constitute the accuracy and

---

* The reason for the varying interfacial tension coefficients in Table 1 is explained at the end of the Numerical Methods section.

efficiency of the solvers stemming from the Featflow solver family, which has already proven its accuracy and performance in solving numerous numerical benchmark problems (Hron and Turek, 2006, Damanik et al., 2010, Hysing et al., 2009, Bayraktar et al., 2012).

The here applied computational strategy including a detailed validation procedure is based on the previously published work in Turek et al. (2019) and Mierka and Turek (2021). In the following we point out only the main features of the mathematical model and the respective numerical framework taking advantage of direct numerical simulation (DNS) of the corresponding multiphase flow problem in the framework of an interface tracking (IT) approach, which requires a transient direct resolution of the gas-liquid interface by the computational mesh. The resulting set of equations established in the context of generalized multiphase flow is as follows:

$$\left.\begin{array}{c} \rho(\mathbf{x}) \left[\frac{\partial \mathbf{u}}{\partial t} + \mathbf{u} \cdot \nabla \mathbf{u}\right] - \nabla \cdot \left(\mu(\mathbf{x})[\nabla \mathbf{u} + \nabla \mathbf{u}^T]\right) + \nabla p = \rho(\mathbf{x})\mathbf{a}_g + \mathbf{f}_\Gamma(\mathbf{x}, t) \\ \nabla \cdot \boldsymbol{u} = 0 \end{array}\right\} \tag{6}$$

where $\mathbf{a}_g$, $\rho(\mathbf{x})$ and $\mu(\mathbf{x})$ represent the gravitational acceleration, density and viscosity and of the respective phases. These two latter depend on the respective interface Γ separating the liquid and gaseous phases. In addition, the surface tension force $\mathbf{f}_\Gamma(\mathbf{x}, t)$ is activated at the resulting dynamic interface, which is defined as follows:
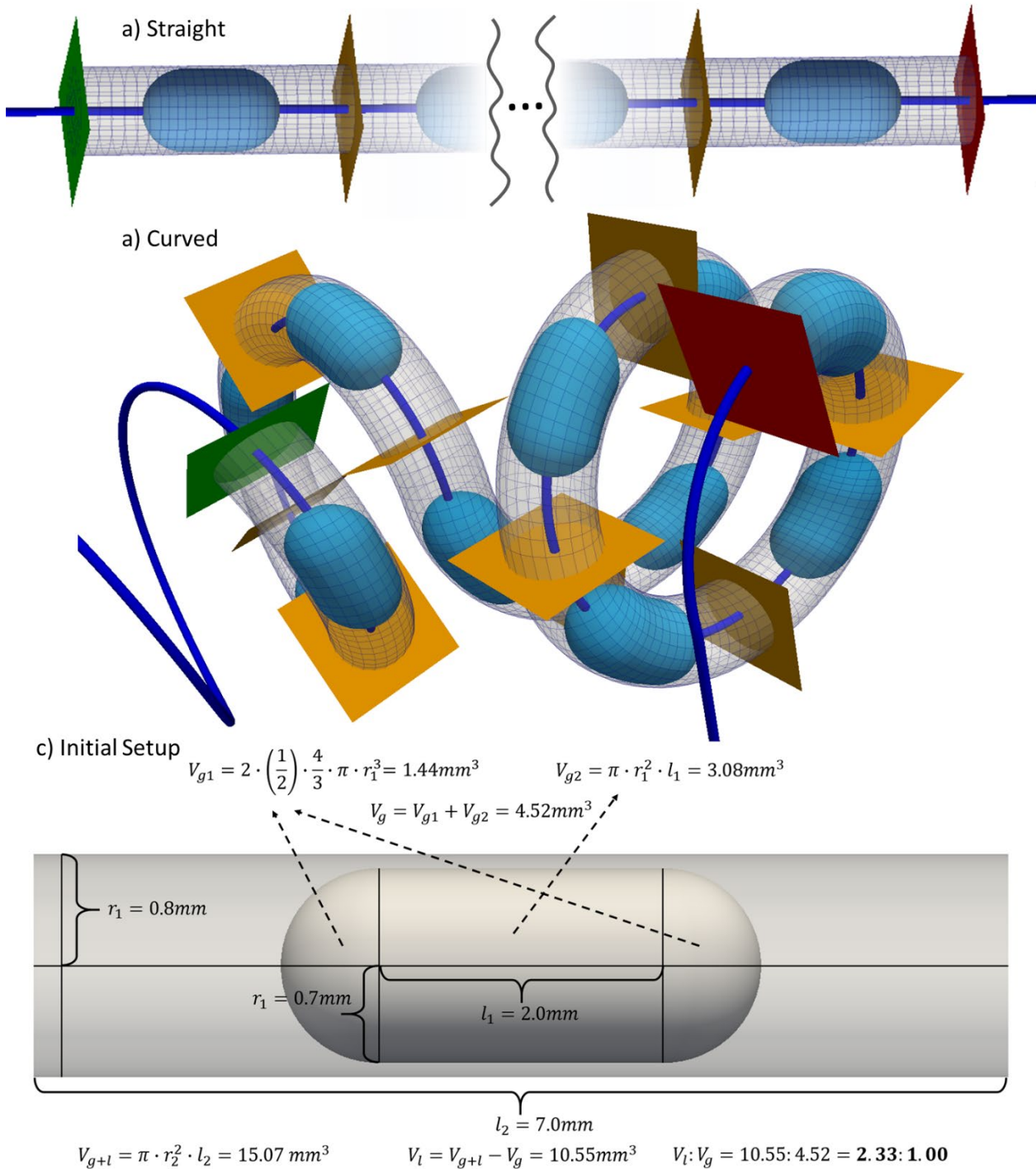
$$\mathbf{f}_\Gamma = \sigma_{l/g} \kappa \, \mathbf{n}_\Gamma \tag{7}$$

where $\sigma_{l/g}$, κ and $\mathbf{n}_\Gamma$ each stand for a certain (material-dependent) interfacial tension coefficient, the curvature and the outer normal to the interface Γ. The resulting nonlinear system of equations is therefore defined for the quantities $\mathbf{u}$ (velocity) and p (pressure).

The presence of multiple phases and the interface between them implies the need for an additional transport equation that controls the deformation of the computational mesh with respect to the effective transportation of the computational domain through the CFI geometry and due to the dynamically evolving interface Γ. Therefore, the two-phase computational model with the arising free interfaces are combined with the interface tracking approach, so that the system of equations defined above is completed by the mesh deformation (MD) equation (which controls the motion of the computational mesh) for the displacement vector *d,* as follows:

$$\nabla \cdot (\nabla \mathbf{d} + (\nabla \mathbf{d})^T) = 0 \tag{8}$$

which is to be augmented by case specific boundary conditions, so to guarantee a secure and successful run of the individual simulations. The corresponding graphical sketch displaying the necessary components for the application of suitable boundary conditions is provided in Figure 6.

a) Straight

a) Curved

c) Initial Setup

$$V_{g1} = 2 \cdot \left(\frac{1}{2}\right) \cdot \frac{4}{3} \cdot \pi \cdot r_1^3 = 1.44mm^3 \qquad V_{g2} = \pi \cdot r_1^2 \cdot l_1 = 3.08mm^3$$

$$V_g = V_{g1} + V_{g2} = 4.52mm^3$$

$r_1 = 0.8mm$

$r_1 = 0.7mm$

$l_1 = 2.0mm$

$l_2 = 7.0mm$

$$V_{g+l} = \pi \cdot r_2^2 \cdot l_2 = 15.07\ mm^3 \qquad V_l = V_{g+l} - V_g = 10.55mm^3 \qquad V_l{:}V_g = 10.55{:}4.52 = \mathbf{2.33{:}1.00}$$

Figure 6: Transformation of the computational mesh from the a) straight into the b) curved representation. Dark blue stands for the centerline, light blue represents the gas-liquid interface, orange shows the intercompartment planes, red and green stand for the inflow and outflow planes and the transparent mesh surface corresponds to the outer capillary wall, here the example for the simulation setup Geo1. Subfigure c) displays the geometrical representation of the initial generic bubble/slug with the resulting volume fractions.

These boundary conditions ensure that the mesh deformation takes place in every compartment (air bubble + liquid slug) individually, without influencing the neighboring compartments. This is achieved by an explicit prescription of the mesh-vertices' displacements (in form of transient Dirichlet boundary condition) at each

of the compartment separation planes in form of a plane equation aligned normal to the centerline of the underlying CFI geometry at a particular position. The position of all these compartment separation planes is determined by a parametrized centerline position, in particular, all these positions are calculated as midpoints (also in parametric sense) between the respectively parametrized bubble front and bubble tail positions. According to this strategy it is possible to address all the intercompartment plane boundary conditions. The parametrization of the remaining inflow and outflow planes is prescribed by the help of the first and last intercompartment plane by a relative (positive or negative) parametrized displacement of the underlying compartment length. For clarity, it is worth to note that the inflow plane with the respective inflow flow profile is advected along the CFI centerline parametrization so that its magnitude is always constant, but the direction is every time aligned with the respective CFI centerline direction. Subsequently, the velocities (referred to as *average velocity* in Table 1) are quantifying the average liquid velocity for the such imposed liquid phase inflow boundary condition.

The key item in regards of the here developed parametrization technique is obviously the CFI centerline which in our case was adopted to be available in a discretized multi-line segment representation. Accordingly, the parametrization of any point inside of the overall computational domain was reduced to a simple computation of the closest line-segment of the centerline followed by a subsequent projection of the analyzed point into the found line-segment, see Figure 6.

The other boundary treatment of Eq. (2) is subjected to the free interface, which is aligned with the mesh and parametrized with three-dimensional Q_2 elements in form of a set of quadrilateral faces. The mesh vertices related to these faces are to be projected on to the surface predicted by the old interphase point locations advected by the determined velocity components $\boldsymbol{u}^{n+1}$ of the respective vertices forming the topological representation of the interface and thus the continuous representation of the interface. To be more precise, only the tangential-free components (with respect to the interface-normal) of the velocity are used for the new-interface update. It is important to note, that the such obtained new surface vertices provide only the necessary geometrical parametrization of the interface, but the particular position of the interface vertices is determined by the mesh-deformation equation (Eq. (8)), as follows. Accordingly, the mesh-deformation equation is solved in a 2-step prediction/correction fashion, first the interface nodes are not subjected to any (internal) boundary treatment (prediction step), instead, the such obtained vertex positions are projected onto the already mentioned geometrical parametrization of the gas-liquid interface, and therefore in the second step these vertices are frozen (subjected to Dirichlet boundary treatment) so that the gas- and liquid-phase vertices can adapt to the determined deformations caused by the updated intercompartment plane positions and the gas-liquid interface positions, respectively. The last boundary treatment involves the outer wall surface of the CFI, which is, however, treated in the very same way as the gas-liquid interface itself with that difference that the Q_2 element-based surface representation for this

boundary is stationary (constant in time), and therefore initialized in the beginning of the simulation and is not subjected to any updates (in contrary to the previously described gas-liquid interface treatment).
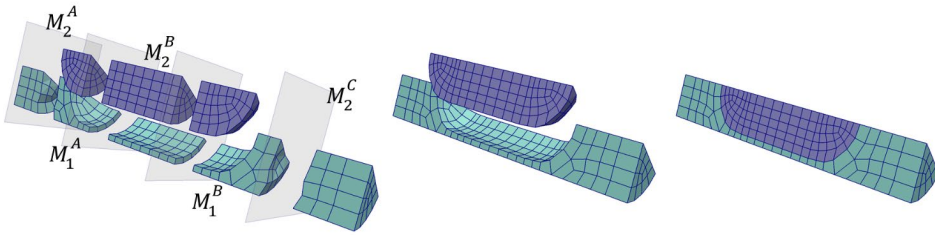
Figure 7: Basis of the generic mesh generation strategy. Left subpicture displays the subdomains $M_1 = M_1^A \cup M_1^B$ and $M_2 = M_2^A \cup M_2^B \cup M_2^C$. The particular geometric realization of the subpieces is merged together in the middle subpicture. Right subfigure displays the mesh regions representing the gas and liquid phases and as required from the underlying IT approach a mesh-conforming representation of the interface.

Despite of the complexity of the underlying CFI simulations there is a huge potential for designing of an automation mechanism for generation and execution of tailored simulation setups, and therefore we find it to be useful to mention some additional practical realization details, so to make it possible to investigate a larger parameter space in which numerical simulations might be performed in order to extend the focus of engineering analysis. The basis for such an automation mechanism is a two-way transformation tool, which allows the transformation from a Cartesian coordinate system into the coordinate system of the CFI and vice versa. Subsequently, a basic computation mesh is to be (in our case a hexahedral) constructed by means of only 2 sub-pieces, where one subdomain corresponds to the head or tail of the gas bubble (requires a 3D unstructured mesh) and the second subdomain, which makes it possible to initialize specific gas-liquid fraction setups (see Figure 7). This second subdomain is therefore subjected to an extruded topological structure (only 2D unstructured mesh) so to increase or decrease the volumetric fraction of the gas-bubble or the liquid slug. These basic mesh-structures are to be generated as pie-pieces, so that in case of necessity they can cover a 30°, 45°, 60° (or any suitable pie piece) so to periodically generate the respective 360° sample, which is then to be multiply connected along the straight capillary axis. This strategy is necessary for guaranteeing the resolution of the thin film between the gas-liquid interface and the capillary wall in the circumferential direction of the capillary. Note that, for large surface tension effects (slow transportation speed, large interfacial tension coefficient, large curvature of the CFI, etc.) the thin film thickness might drastically decrease and even the isoparametrically parametrized Q_2 elements might got corrupted, or might drastically deteriorate the convergence rates of the simulation, which might be compensated up to a certain extent with a larger number of mesh-pie pieces in the circumferential direction.

In the next instance this straight structure is to be transformed with the transformation tool into the curved representation, while assuring the availability of a suitable number of gas-liquid slugs front of the 2π inflow coil so to guarantee the achievement of a periodic flow structure while pressing the gas-liquid compartments

through the CFI structure. These redundant liquid slugs represent a "slug buffer" the number of which is quite strongly dependent on the overall Re number. The higher the Re number the more buffer slugs are necessary, since the achievement of periodic behavior requires a larger time span of simulation time. During the transformation process (from straight to curved) it might be necessary to propagate the respective face representations for the prescription of the respective boundary conditions during the simulation, such as the set of faces corresponding to the individual gas-liquid interface or to the inter-compartment plane representations.

It should be noted that due to the chosen IT approach, the underlying computational mesh is subjected to a constant topology throughout the whole simulation. Only the coordinates of the individual mesh vertices are changing, first due to the effective transportation through the CFI and due to the additional deformation of the gas-liquid interface, which leads to an overall mesh speed ω, giving rise to the ALE treatment of the mesh motion. Another essential feature of the here used IT approach is the resulting semi-implicit treatment of the surface tension force by exploiting the Laplace-Beltrami transformation following the work of Hysing (2007). The surface tension force is introduced into the momentum equation as a surface integral in the FEM discretization for the IT approach in the following form:

$$\mathbf{f}_{st} = \int_{\Gamma} \ \sigma \kappa \mathbf{n}_{\Gamma} \cdot \mathbf{v} \, d\Gamma \tag{9}$$

which is according to the Laplace-Beltrami transformation expressed by the help of tangential surface derivatives $\underline{\nabla}$ and $\underline{\Delta}$ including partial integration, as follows:

$$\mathbf{f}_{st} = \int_{\Gamma} \ \sigma \big(\underline{\Delta} \, \mathbf{x}|_{\Gamma} \big) \cdot \mathbf{v} \, d\Gamma \tag{9} \tag{10}$$

Since the new interface position $(\underline{\Delta} \, \mathbf{x}|_{\Gamma})(n+1)$ can be expressed as a function of the old interface position, the surface tension term can be represented in a semi-implicit way by including its contribution in the transport operator A and on the right-hand side of the Navier-Stokes equation. In this context, it is important to note that the surface tension is provided element-wise as a surface integral by using the isoparametric geometric mappings, which allows accurate sampling of the curvatures at the corresponding integration points. Since all the listed equations defining the treated problem are coupled in a strongly nonlinear way, their solution requires a numerically robust and efficient solver. Therefore, the solution of the resulting system is subjected to a decoupling solver mechanism inspired by the discrete projection (DP) method. According to the applied DP method, the solution of the system is decomposed into individual solution steps, as already presented by Mierka and Turek (2021). A typical representation of a solution result and the respective resolution of the computational mesh is given in Figure 8.
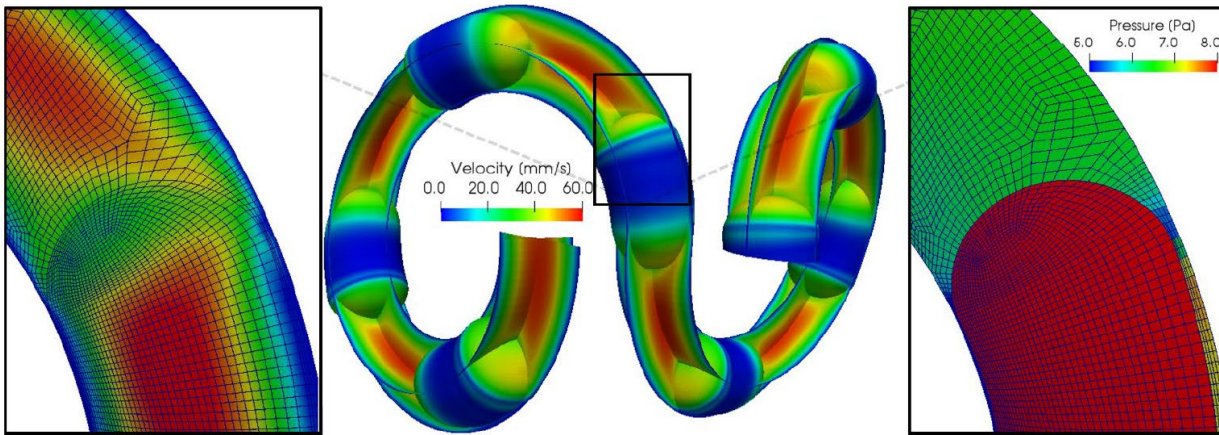
Figure 8: Typical simulation result of the CFI Taylor bubble for the simulation case Geo1/Op1 showing the interface aligned mesh. The close-ups show the respective velocity distribution and the resolved pressure jumps on the respective sides of the interfaces. Note, that the irrelevant buffer regions located at the inflow and outflow section of the geometry have been clipped away from the middle subfigure thus showing only the relevant $2\pi + \pi/4 + 2\pi$ part of the computational domain.

The reverse usage of the transformation tool (transforming coordinates from the curved geometry back to the straight counterpart) receives a central role in the mixing analysis. At these postprocessing particle tracing simulations the particles are injected into the inflow plane (parametrized centerline position 0.0) into the individual quadrants of the inflow coils which are then traced until leaving the computational domain (parametrized centerline position $2\pi + \pi/4 + 2\pi$). The seeding of the particles happens at that instance when the intercompartment plane of the 2 closest compartments coincides with the inflow plane **and** the periodicity of the flow has already been reached (the last 2 revolutions do differ only up to the prescribed tolerance). During the particle tracing simulations, all particle trajectories are to be stored so that by using the reverse transformation tool all these intermediate locations can be transformed back to the straight representation. Analysis of the particle dynamics in the straight representation allows those unconventional characterizations, which reveal the particle mixing patterns in the angular direction of the capillary. These methods are allowing for a performance quantification of the 90° bend distinguishing the CFI geometry from a simple coil.

The here described computational method is subjected to robust numerical properties allowing its application for a rather challenging geometrical realizations involving a sequence of several gas bubble/liquid slug pairs, however, it is also conditional to certain limitations which deserve to be clarified. The only serious numerical restrictions are related to the following aspects:

- *Topology*: Due to the fixed mesh topology the bubbles are not allowed to break up, coalesce or diminish the liquid film between the gas bubble and the capillary wall.
- *Periodicity*: Due to the subsequent particle tracing based mixing quality analysis it is inevitable to obtain a periodic flow pattern in the underlying CFI geometry which depending on the operation conditions might experience different time scales (computational time is increasing for increasing Re).

- *Stability*: Due to the combination of the CFI curvature, transportation speed (speed of the liquid or gas phase) and interfacial tension it might happen that the resulting liquid film between the gas bubble and the capillary wall becomes so thin that its resolution would require such an (a priori constructed) fine mesh which would result in an extreme amount of computational resources.

From these computational restrictions only the last one had to be artificially adjusted so to circumvent unrealistically expensive computational scenarios. However, the value of interfacial tension coefficient was relaxed only in an interval so that the resulting liquid film thickness in all analyzed cases was below 1.5% of the capillary diameter.

4. Hydrodynamics of 2-phase flow in the CFI

To investigate the complex flow behavior of gas-liquid Taylor bubble flow in coiled capillaries with 90° bend with inlet and outlet effects, the simplest but reasonable and meaningful setup was chosen. The helical capillary starts with 360° turn, a 90° bend and a second 360° turn as basic geometry, see Figure 5. Typical values inner diameter and coil diameter are given in Table 1.

The fluid parameters are as follows for the liquid (water) and gas (air) as continuous and disperse phase, respectively: The density of liquid and gas is 1000.0 kg m^{-3} and 1.2 kg m^{-3}, respectively, as approximate values for ambient conditions (1 bar abs and 20 °C). The viscosity of liquid and gas is 1.12 mPas and 0.018 mPas, respectively. The surface tension σ had to be decreased from the 20 mN m^{-1} to only 2.5 mN m^{-1} due to numerical stability reasons. The bubbles flow with a velocity of 3, 6, and 12 cm s^{-1}, which leads to a liquid Reynolds number Re of Re = 42.86, 85.71, and 171.43, respectively. The phase ratio of liquid to gas is approx. 2.4:1.0 with a bubble length of approx. 2.5 mm and a respective bubble&slug segment length of approx. 6.0 mm.
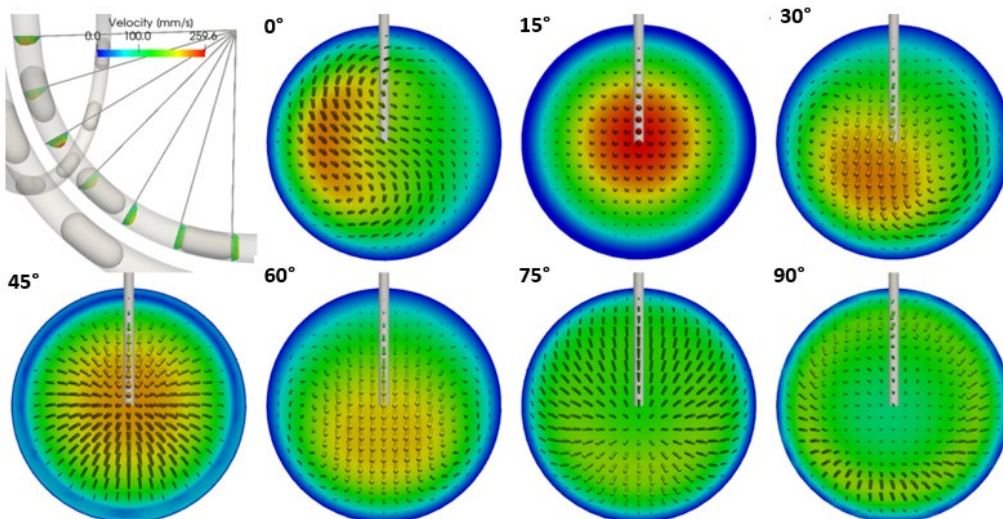

4.1. Velocity distribution in a cross section

Figures 9 and 10 show the results of the hydrodynamic investigation of Geo3 for two different flowrates (Op1 and Op3). The velocity arrows with a gas-liquid flow are shown in the capillary cross section at different positions in the curvature just after the 90° bend. In Figure 9, the flow velocity reaches a maximum of $u_{1,max}$ = 65 mm s^{-1} in the parabolic velocity profile of the liquid phase with an average flow velocity of $u_{1,mean}$ = 30 mm s^{-1}. In Figure 10, the maximum velocity reaches a value of about $u_{2,max}$ = 260 mm s^{-1} with the parabolic velocity profile of the liquid phase with a mean flow velocity of $u_{2,mean}$ = 120 mm s^{-1}.
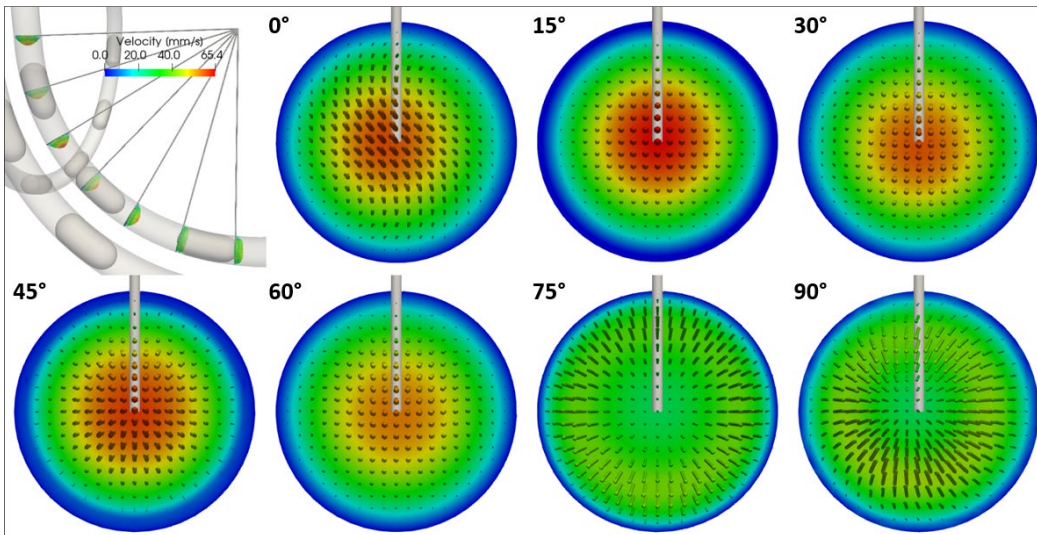
Figure 9: Visual decomposition of the Geo3/Op1 simulation result in the 90° bend cross sections. Velocity distribution of continuous phase (water at 0°, 30°, 60°, 75°, and 90°; gas at 15° and 45°). The arrows represent the velocity vectors in the respective cross sections.

The comparison of the Figures 9 and 10 shows the influence of the centrifugal force on the flow velocity distribution. At low velocities, as present in Figure 9, the resulting centrifugal force acting on the fluid is not sufficient to affect the flow profile. The maximum velocity remains centered in the capillary as shown by the cross sections at 30° and 60°. In Figure 10, on the other hand, the flow velocity distribution in the cross section of the liquid phase at 0°, 30°, and 60° shows a shift of the velocity profile in the direction of the centrifugal force. At 0° position, the maximum velocity is located left hand side from the center, as remaining from the helical curvature before the 90° bend.

Figure 10: Visual decomposition of the Geo3/Op3 simulation result in the 90° bend cross sections. Velocity distribution of continuous phase (water at 0°, 30°, 60°, 75°, and 90°; gas at 15° and 45°). The arrows represent the velocity vectors in the respective cross sections.

Directly at the 90° bend, the maximum flow velocity is located at 9 o´clock, which origins from the helical flow in the first coil. The 30° cross section shows the already counterclockwise moved flow profile with

maximum flow velocity at 7 o´clock. The cross section at 15° indicates the flow velocity profile of the gas phase with virtually no influence of the centrifugal force resulting in a central point symmetry profile. At 60°, the liquid flow profile is shown just in the front of a gas bubble with less pronounced maximum velocity. However, the maximum velocity is located in the direction of the centrifugal force indicating a developed flow at this point already. Finally, the cross sections at 75° and 90° are directly before and after a gas bubble and show more outward and inward directed flow direction, respectively.

Different attempts with streamlines failed to display the complex three-dimensional flow in the continuous phase under centrifugal force influence. In addition, the flow situation in the 90° bend and the successive length is not illusively depictable with streamlines due to the dynamic situation. In the following, a particle tracking approach is chosen to illustrate the flow characteristics and dispersion behavior.

4.2. Hydrodynamics by particle tracking

Particle tracking is a common technique to visualize flow characteristics in a time-dependent manner. Here, the laminar flow profile and its deflection is visualized. Further the dispersion process due to two-phase flow in capillaries as well as the influence of the 90° bend on the dispersion is optically shown, but also statistically evaluated with the position of certain particle starting in a defined sector of the cross section. With this method, the dispersion and mixing process leading to a narrow residence time distribution in the CFI is explained and elucidated for the first time.

As the full 3D flow in CFI capillaries exhibit no symmetry and repetitive flow structures, it is not possible to construct streamlines. Hence, particle tracing in a CFI geometry with a series of 'large' Taylor bubbles is a viable method for getting more information from the flow field, see Figure 11.

The particle tracking is arranged with the following starting conditions:

1) initial particle seed at t = 0 on an already developed flow field in the middle of the continuous phase between two gas bubbles,

2) cross-like segregation in centrifugal symmetry with inner left and right (blue and yellow) and outer part (red and green), respectively, in view direction of flow.

The seed is imposed in a way to separate the particles from the different quadrants of the capillary and to visualize the flow behavior with time (or space). Starting points are given in SI, Figure SI-1.
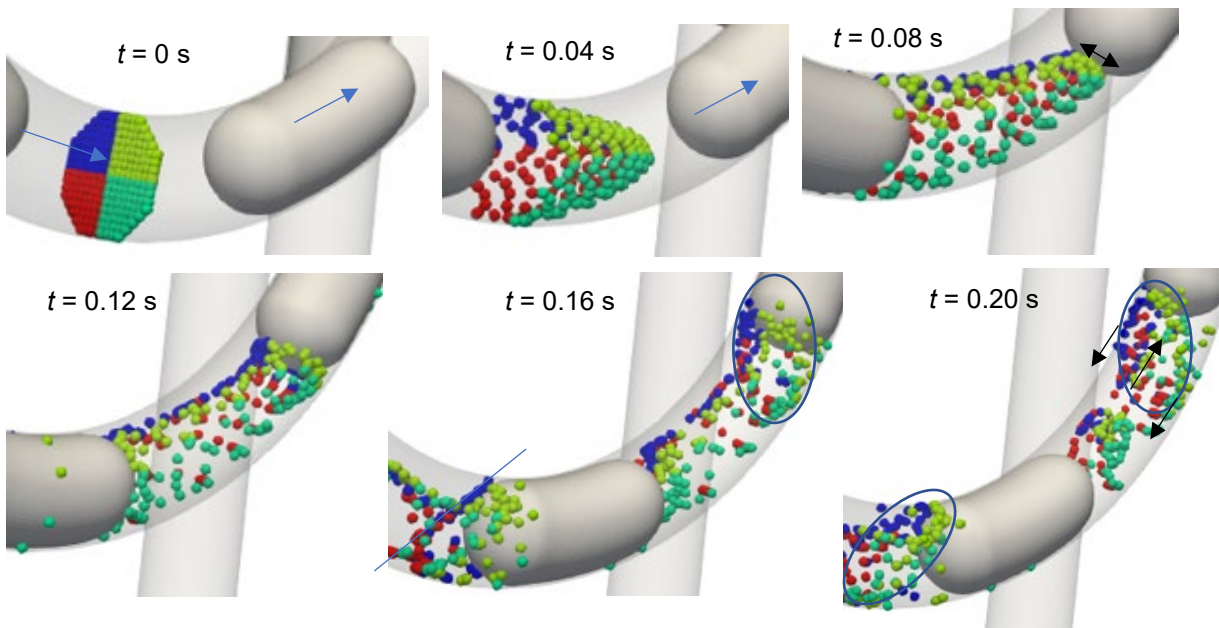
Figure 11: Particle tracing visualization of the superimposed Taylor-Dean flow structures in the continuous phase located in the helical part of the CFI for the simulation case Geo2/Op1.

At t = 0.08 s, the first particle in the core flow reaches the front bubble, while the particles at the wall are captured by the wall film of the rear bubble. The asymmetry of the parabolic flow profile is of approx. 16.7 % deflection from center axis after 2.4 mm of flow distance. At t = 0.12 s, the asymmetric circle at front cap is close to the outer wall, and a recirculation at the stern of the continuous phase leads to a particle collection at rear cap. Single particles attach at the wall indicating the thin wall film flow. At t = 0.16 s, the backflow in the front area has an ellipsoidal shape, while even more particles are collected in the rear. In the last image at t = 0.20 s, the front particles form an inclined ellipsoid, while the particle at the rear are collected in the center flow and stream forward.

From the above observations, the following areas can be derived of investigations in particle mixing. One area is to follow a radial cross section along a 360° turn and 90° bend, while observing bubble velocity to understand particle mixing. Another approach involves exploring different starting points of a cross section to follow a 360° turn, a 180° turn, a 90° bend, and another 180° turn. Additionally, comparing an axial cross section with experimental work, specifically the concentration profile of leuco-indigo carmine in the work of Schlüter et al. (2021) can provide valuable insights. These investigations aim to deepen our understanding of particle mixing in various flow scenarios and potentially enhance related experimental techniques.

5. Particle dispersion in two-phase CFI flow

5.1. Starting considerations of particle dispersion

The particle dispersion is investigated with a slug filled with differently colored particles with different starting positions. In a first step, four quadrant volumes separated by the symmetry axis of the centrifugal force and inner / outer region were investigated regarding their different dispersion behavior. The cross-like structure is depicted in Figure SI-1 with red and yellow particles in the outer left and right region, respectively, together with green and blue particles in the inner right and left region, respectively. The particle distribution is given for an observer moving with the front gas slug looking against the flow direction. At slide 60, just after 90° bend, the particle distribution gets chaotic. Before, some regular structures can be observed, however, more detailed investigations are necessary for the entire description of the flow behavior. The qualitative findings and observations are given in the SI.

The numerically obtained periodical solutions have been extracted for the subsequent mixing performance analysis by utilization of a (massless) particle tracing initialized by particle seeds in 4 quadrants of the first liquid slug as shown in Figure 12. For the postprocessing of these particle tracing results the same transformation method has been utilized, however, this time in the inverse direction. The such transformed data made it possible to compare and characterize the dynamic particle distribution within the physical geometry (Figure 12 a)) in the angular direction (Figure 12 c)) and along the axial direction (Figure 12 b)) of the "backtransformed" straight capillary. Such a particle distribution reconstruction for the four initial particle seeds is demonstrated in 3D-display of the particle positions. The reconstruction is clearly addressing the justification of the 90° bend, which substantially contributes to enhanced mixing of the liquid slug.
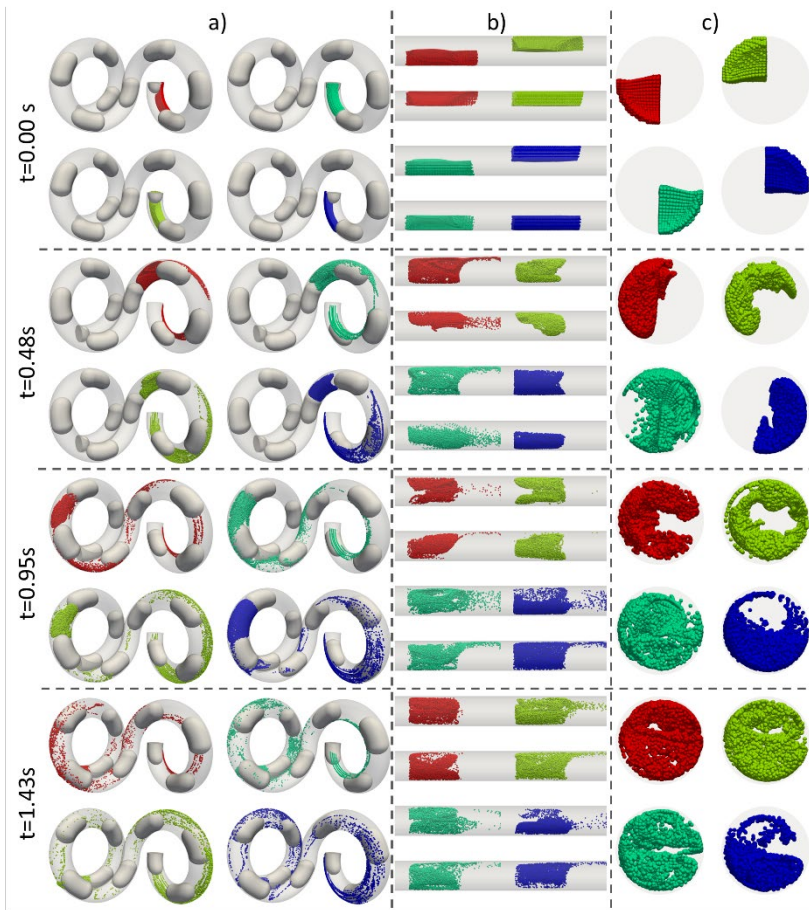
Figure 12: Mixing analysis simulation with the use of particle tracing method demonstrated for the simulation case Geo1/Op1. The leftmost sequence (a)) shows the particle dynamics in the physical geometry. The middle (b)) and right (c)) sequences show the particle dynamics in the "backtransformed" geometry (with straight capillary display) in the axial (b)) and cross-sectional (c)) direction by tracking the initially seeded liquid slug segment. The evolution of the particle distribution is visualized in the top-to-bottom direction for the time levels 0.00 s, 0.48 s, 0.95 s, and 1.43 s. For details, the reader is referred to SI and to the linked animations.

In the cross-sectional images, the particles are observed from the front part against the flow direction. It is important to establish a convention for particle orientation. Yellow and red particles are mainly found in the inner half, while green and blue particles are located in the opposite part. Only few red and blue particles cross the interface and move within the front bubble. The particle quarters experience centrifugal and torsion forces, particularly the yellow particles, which start on the inner side and are affected by an "opening" torsion effect. As a result, they are distributed asymmetrically over the half circle, followed by the red particles. Particles that start from the outer position have more restricted mobility and are distributed over the half circle just before the 90° bend. The blue particle exhibits an interesting secondary vortex that extends to the opposite half, forming a "jet" just before the 90° bend. After the 90° bend, chaotic mixing occurs, resulting in a very good distribution of all particles across the entire cross section. The red particles form a U-shaped distribution until the end of the second helical coil. Following a 360° initial turn, 90° bend, and another 360° turn, all segments of particles are distributed evenly across the entire cross section and no longer exhibit any regular structure. A refined statistical investigation will give a detailed picture in the following.

5.2. The 2-dimensional representation of particle position and dispersion

The particle position in the cross section gives only a qualitative impression of the dispersion. To get quantitative values, the position of the particles with different color from related starting position are evaluated with a histogram, indicating their angular position. The radial coordinate is assumed to be of secondary importance, since the particles are ordered in sections with their angular position and with different radial coordinates. Here, the number of particles with a certain angle from the center is indicated with the height of the bars. At the starting point, all four quadrants result in a block-like bar distribution in the histogram. In Figure 13, the temporal development is shown for the particles starting in the four segments. Until 2.3 sec in slide 60, the first turn is passed, however, nearly all the particles stay in their respective half, given by the symmetry of the centrifugal force, then, the 90° bend serves for further distribution over the complete cross section.
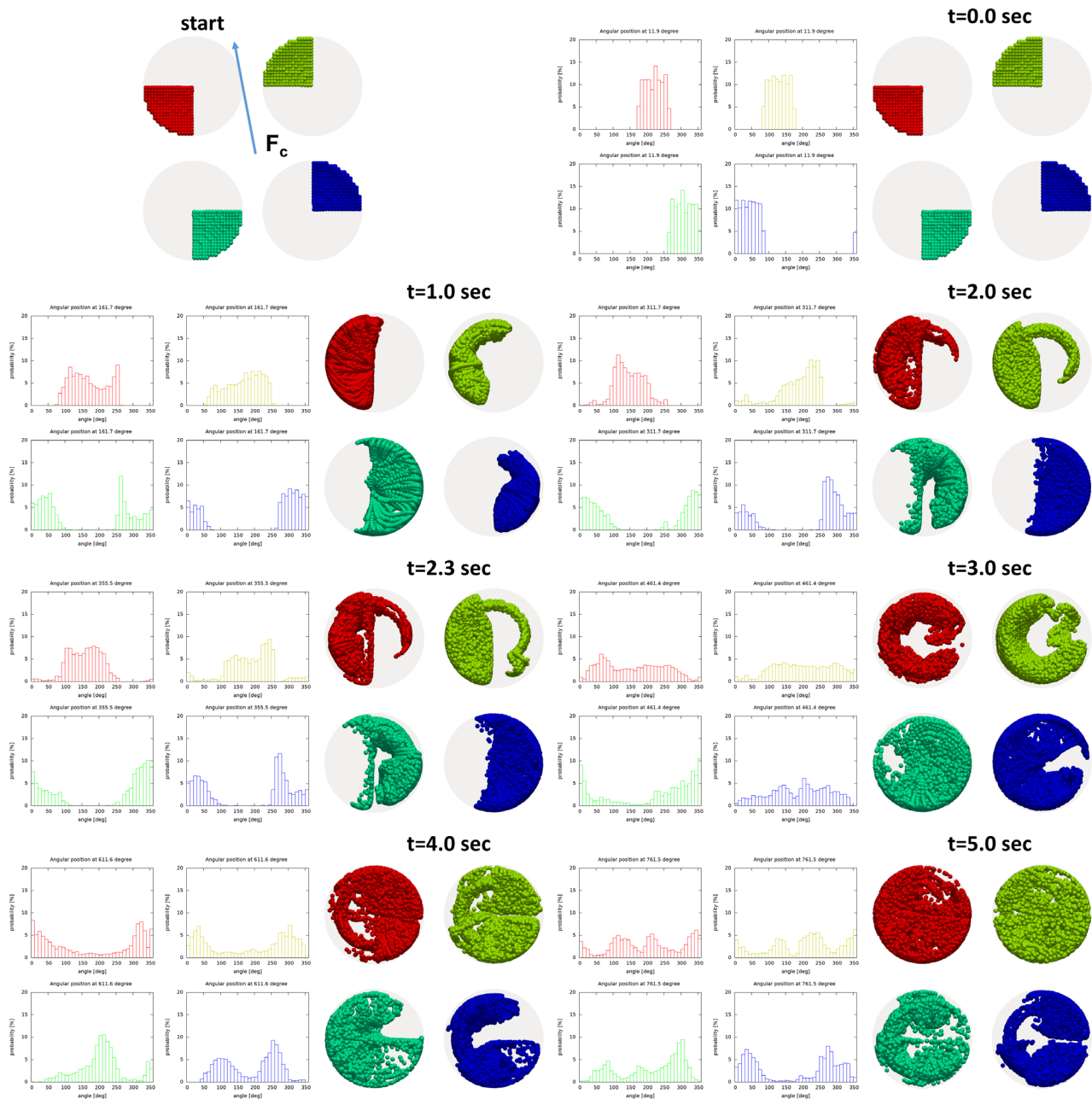
Figure 13: Particle position due to fluid dispersion in histograms along the simulated CFI corresponding to case Geo3/Op1. Section-wise particles in green, yellow, blue, and red for flow visualization. The direction of the centrifugal force is given with the blue arrow.

The four different colored particles behave differently in detail, but some similarities can be observed. After 1 sec, the green and red particles occupy nearly the half circle of the starting point, while yellow and blue are still distributed in a smaller volume. After further 1 sec. the particles of all colors are spread over their cross-sectional half, where green and red already reaching into the opposite half. After further 1 sec (3 sec), all particles are spread over the entire cross section due to the 90° bend. After 5 sec in total, the red and yellow particles are covering the entire cross section, while the green and blue particles exhibit a more or less strict horizontal symmetry plane. The related histograms show a quite even distribution of the green and blue particles with three maxima, respectively. The distribution in the histograms of the red and yellow particles

after 5 sec shows a less homogeneous distribution over the angle. However, the optical distribution of the particles over the cross section is misleading, hence, further means of particle distribution of the dynamic process is necessary, which is shown in the next section.

The timely development can be seen in the animations (see SI) and with the histograms in Figure 13, but the quantitative evaluation needs other measures. The histograms for each time step are combined in a 3D diagram indicating the development, integrated values in 2D diagram.

5.3. Numerical aspects of quantification of particle dispersion

The analysis of particle dispersion is based on the statistical evaluation of the carefully generated particle tracing results. Thanks to the back-transformation mechanism, all particles at all time levels were transformed back to the straight representation, where they were assigned into the respective angular compartments depending on their angular position. The 360° overall angular space was chosen to be resolved by 36 compartments (10° for each compartment). Accordingly, the histogram of all particles (such as the individually colored particles) was possible to represent for each discrete macro time level (see Fig 13). The initial particle seed was subjected in each case to that liquid slug which was located at the beginning of the CFI geometry so that the center of gravity of the respective particle cloud (i.e. particles remaining in the original slug) can be evaluated and back-transformed into the straight coordinate system. Since all here analyzed CFI cases were subjected to a $2\pi+\pi/4+2\pi$ segment representation (in-flow coil, inverter bend and out-flow coil) the angular histograms were evaluated against the respectively projected CFI centerline positions, however, not in terms of absolute distance but in terms of the angular parametrization (in terms of the $2\pi+\pi/4+2\pi$ angular interval) so to provide a better relative comparison between the different geometries. Such graphical evaluations are displayed in Fig 14, 15, 16 and 19. In particular, the data displayed in Fig 14 is subjected to a subsequent variance evaluation which is simply the standard deviation of the angular probabilities over the 36 compartments in each discrete macro time level projected to a respective CFI angle position within the $2\pi+\pi/4+2\pi$ angular interval.

5.4. Particle dispersion development along the CFI

The position of the individual particle can be tracked along their flow in the CFI. In particular, the angular position is interesting for the dispersion, since the axial position is determined by the liquid slug. In Figure 14, the variance in the angular position of the four different particle fractions is displayed over the CFI length. High variance value means the agglomeration of particles in a certain corner of the cross section, while a low number indicates a homogeneous distribution over the cross section. The 90° bend between two turn is located between 360°-450°. From the variance, the mixing quality α can be calculated according to Kockmann et al., 2006, however, since the maximum value cannot clearly be defined, this operation was not performed.
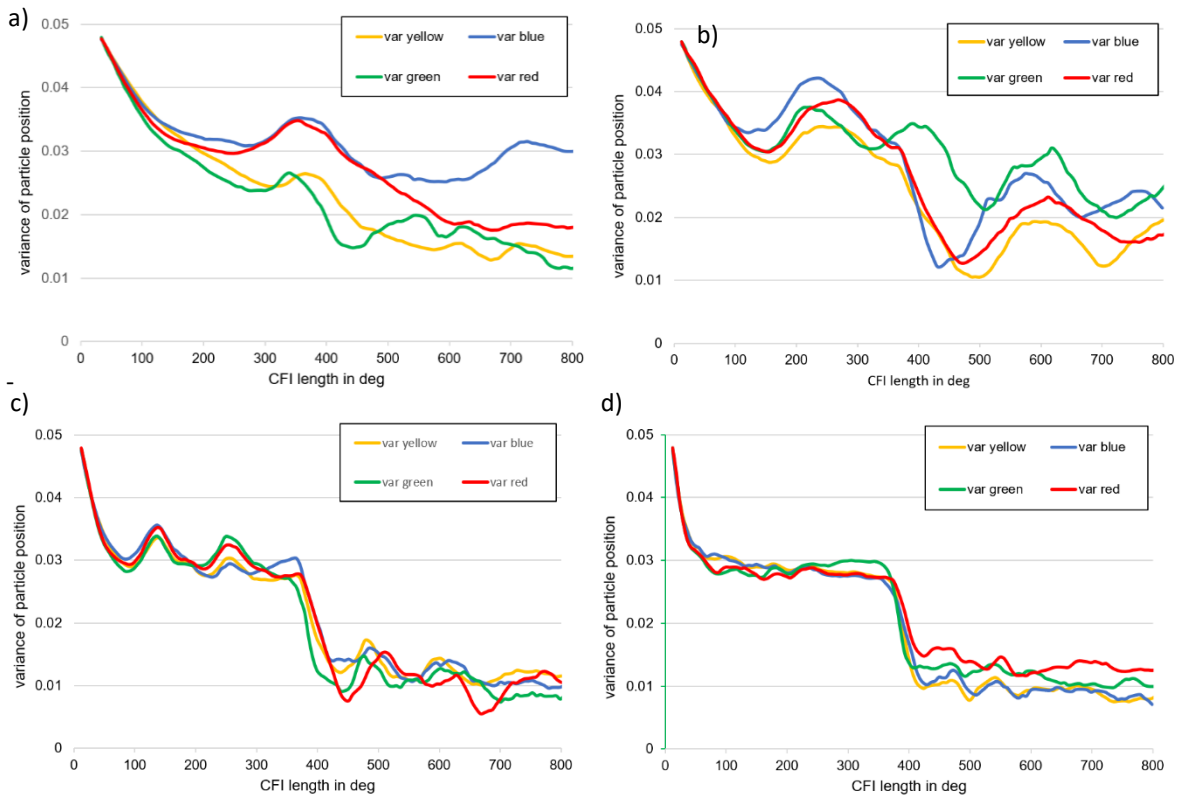
Figure 14: Development of particle position variance along the CFI length, indicating the evolution of particle dispersion for the simulation cases a) Geo1/Op1, b) Geo3/Op1, c) Geo3/Op2 and d) Geo3/Op3.

All curves in the four diagrams in Figure 14 show a decreasing course indicating the continuous mixing due to the Dean vortices. The blue curve in Figure 14 a) for a coil diameter of 6 mm is increasing in the second turn due to the inhomogeneous flow and possible de-mixing of the particles in this particular CFI segment, while the other colors are decreasing. The influence of the 90° bend is only slightly visible in Fig. 14 a), while in all other diagrams, the variance curves are dropping in value after 360°, indicating a larger influence of the 90° bend. The larger drop in Fig. b) compared to a) indicates the influence of the larger CFI coil diameter, which, however, must be evaluated in future with more simulations. With increasing flow velocity (Figure 14 b to d)), the difference between the four colors is decreasing following all the same trend. The mixing effect of the 90° bend is clearly visible in c) and d) with a steep drop after 360° with the 90° bend. A more detailed analysis can be performed only with more simulations of different flow velocities, various diameters and longer CFI geometry. The mixing effect can be visualized with the information of the particle positions, which is discussed in the following section.

5.5. The three-dimensional representation of particle dispersion

The current position of each particle is recorded along the CFI length and displayed over the cross-sectional angle. In Figure 15, the 3D histograms are shown for continuous phase particle flow in the CFI for the simulation case Geo3/Op1. The first 360° show only little dispersion, the particles stay in their starting areas. At 360° with the 90° bend, all particles move across the entire area, in particular the yellow and green

particles. The red particles stay around the 0/360° position, while the blue particle move to the 90-180° position. The red particles have a higher concentration in the upper right corner, while they starting point was in the lower left corner. The blue particles show low dispersion and low influence of 90° bend. Both particle swarms move more or less to the diagonal opposite part of the cross section.
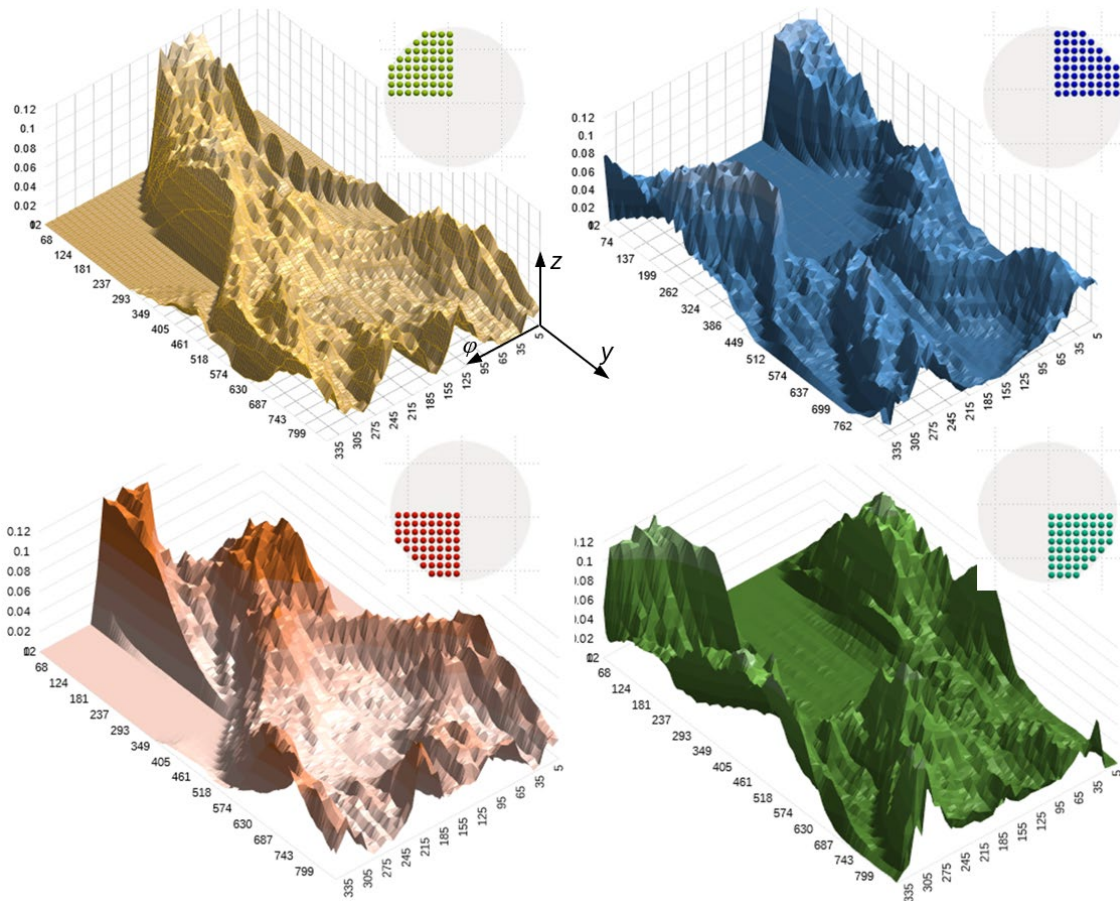
Figure 15: Dispersion visualization via particle probability distribution (z-axis) in angular (φ-axis) and axial (y-axis) direction in the capillary for the simulation case Geo3/Op1.

With smaller coil diameter, leading to higher centrifugal force and higher Dn number, the particle distribution is even less uniform, see Figure SI-3 and Figure 16 with the distribution of the blue particles.
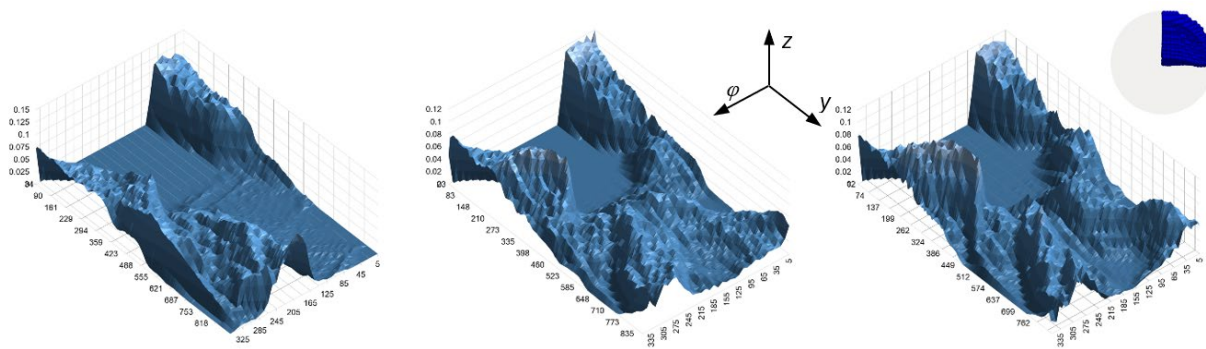

Figure 16: Dispersion visualization in terms of probability distribution for the blue particle seed along the capillary for the simulation cases Geo1/Op1 (left), Geo2/Op1 (middle) and Geo3/Op1 (right).

28

With increasing centrifugal force due to lower coil diameter, the particles in the outer region move to the inner region, but stay at their half side of the cross section. No strong symmetry breaking is observed for the first 360° after the 90° bend. The particles from the other sections show slightly better dispersion, in particular, the good dispersion starts directly with the 90° bend in particular for the inner sections. This steep decline with 90° bend leads to well-mixed regions in the continuous phase. However, the ⊕ arrangement of the particles already introduce an asymmetric starting position related to the centrifugal force. Hence, the starting position of the four colors was changed to a 45° rotated ⊗-arrangement, which distinguishes now between an outer and inner section together with a left and right position in direction of flow. The general information on mixing is not changing with the new particle arrangement, but the flow characteristics can be better described.

### 5.6. Particle starting position in ⊗-orientation

The following Figures 17 and 18 show the positions of particles placed in the capillary. Each quadrant was colored differently. All four quadrants are shown in the figures. The arrow indicates the direction of the centrifugal force, which rotates 90° in the course of the images from a.) to m.) according to the CFI deflection.
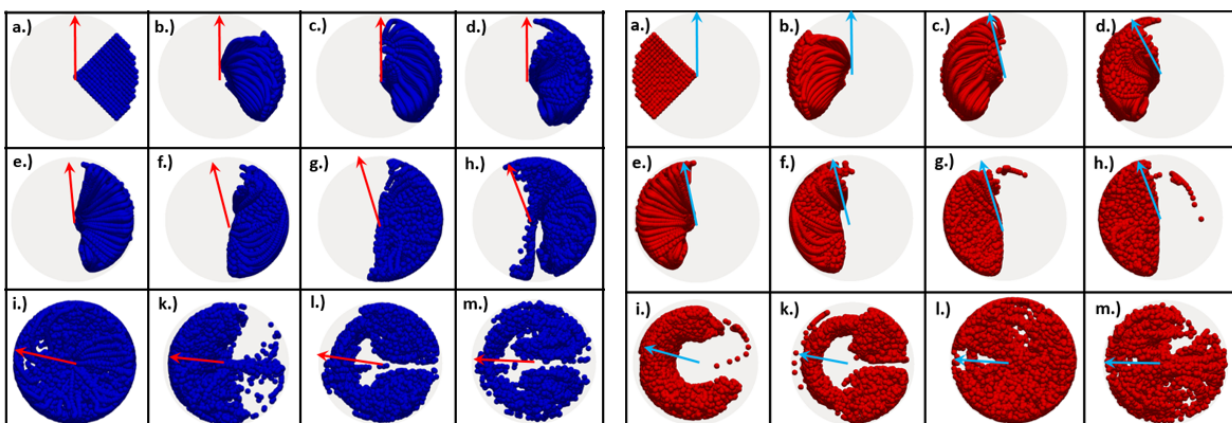
Figure 17: Evolution of red and blue particle distributions for the simulation case Geo3/Op1. The respective blue and red quadrants are opposite to each other. Flow direction is directed towards the observer.

Figure 17 (a.) to h.) shows a very symmetrical behavior for the blue and the red quadrant, as was already observed from the ⊕ arrangement. The shift of the centrifugal force breaks the symmetry axis between the two quadrants (images i.) to m.)). The yellow and green quadrants in Figure 18 are located one behind the other in the direction of the centrifugal force. This means that the yellow particles are initially pressed against the outer capillary wall by the centrifugal force. This leads to a kind of ring formation, with that the particles pressed against the capillary wall are deflected by particles flowing after them along the capillary wall. This behavior can also already be seen in the blue and red quadrants in images k.) to m.).
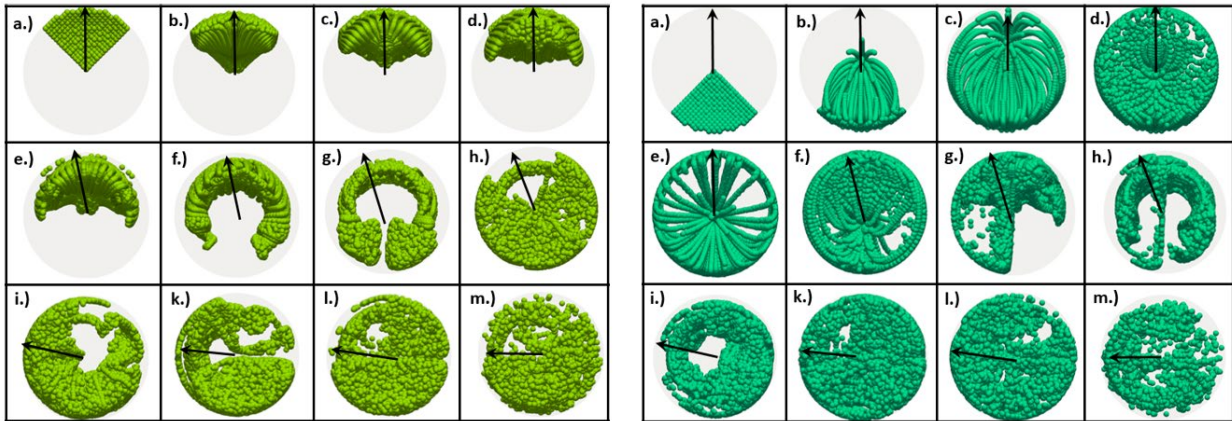
Figure18: Evolution of yellow and green particle distribution for the simulation case Geo3/Op1. The respective green and yellow quadrants are opposite each other.

The particles of the green quadrant quickly distribute themselves already over the entire capillary cross-section, see Figure 18. The special thing about this is that, compared to the other quadrants, there are intermediate areas through which only the particles of one quadrant flow, for example in the pictures e.) to g.). It is to be recognized that there is an area in the middle, which is flowed through only by particles of the green quadrant. This could be the core flow previously observed and described by Schlüter et al. (2021). More information on the axial particle distribution is given in Figure SI-4 with the particle distribution variance along the CFI length.

The histograms of two particle distributions in ⊗ arrangement are shown in Figure 19 for two different velocities. The yellow particles, starting at the outer section, are already well distributed in the first coil after 360°. The higher velocity leads to a very even yellow particle distribution after the 90° bend, which is also valid for the green particles starting in the inner section. The influence of the 90° bend is quite small for both inner and outer section.
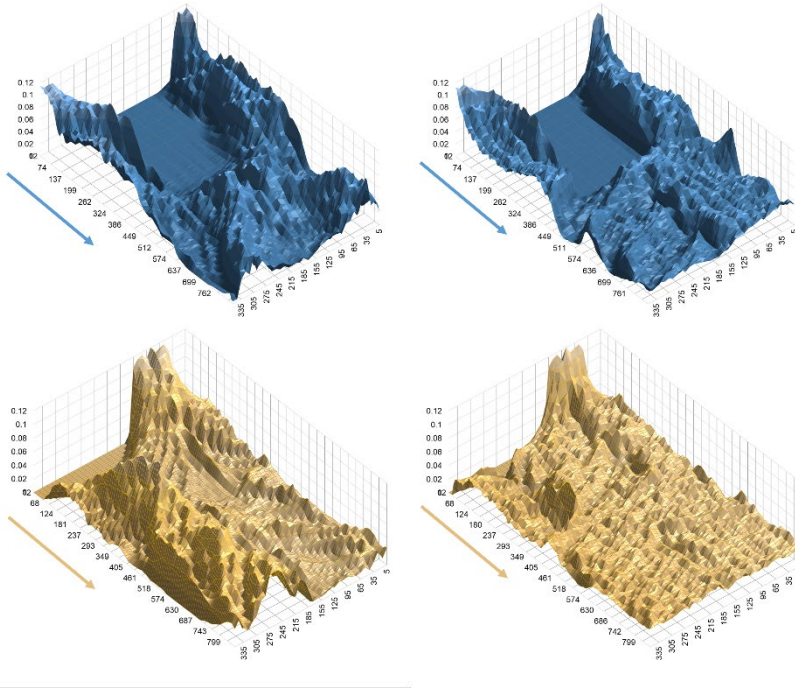
Figure 19: 3D visualization of particle distribution development for the simulation cases Geo3/Op1 (left) and Geo3/Op3 (right).

The side sections show a more stable distribution before the 90° bend, represented in Figure 19 with the blue particles. The blue particles (as well as the red particles) at the right (or left) side of the cross section are still segmented in the first coil. Here, the 90° bend has a large influence on the particle distribution, which is also visible in a steep decline of the mean particle dispersion at the 90° bend, as shown in Figure SI-5. The complete description of the 3D particle distribution for the CFI corresponding to Geo3 is given in the SI with Figures SI-6 to -8. A high flow velocity leads already after two coils and a 90° bend to nearly complete and homogeneous distribution.

6. CONCLUSIONS & OUTLOOK

Two-phase flow in helical capillaries is governed by two different secondary flow phenomena, the Taylor- and the Dean flow, making the numerical simulations difficult. The developed highly accurate multiphase flow model has proven its robustness by its application on the CFI geometry in a wide range of flow parameters. The influence of the individual parameters was revealed on the mixing efficiency of gas-liquid capillary slug flow at already low Re numbers, in particular with the effect of the 90° bend. The here developed transformation method has played a key role in the construction of the periodical fluid domain as well as in the postprocessing analysis focused on flow mixing characterization and parameter comparison. A high flow velocity leads already after two coils and a 90° bend to nearly complete and homogeneous distribution. The coil diameter plays a secondary role, also with its influence on the Dn number. From the presented numerical investigations with particle dispersion, the influence of the coil diameter on the 90° bend dispersion is smaller than the influence of the flow velocity leading to a higher centrifugal force. Due to the high statistical variance

of the particle position distribution, a direct quantitative comparison is challenging and subject to future investigations. Further investigations may include quantitative mixing characterization, e.g. dispersion variance varying with Re and Dn number from mean velocity and helical and tube diameter together with different phase ratio along the capillary length.

7. ACKNOWLEDGMENTS

8. FUNDING SOURCES

REFERENCES

Abubakar, H., Matar, O., 2021. Taylor bubble motion in stagnant and flowing liquids in vertical pipes. Part I: Steady-states. arXiv preprint arXiv:2109.09091.

Akbar, M.K., Plummer, D.A., Ghiaasiaan, S.N., 2003. On gas–liquid two-phase flow regimes in microchannels. Int. J. Multiphase Flow, 29(5), 855–865, https://doi.org/10.1016/S0301-9322(03)00043-0.

Araújo, J.D.P., Miranda, J.M., Campos, J.B.L.M., 2013. Flow of two consecutive Taylor bubbles through a vertical column of stagnant liquid—A CFD study about the influence of the leading bubble on the hydrodynamics of the trailing one. Chemical Engineering Science, 97, 16-33. https://doi.org/10.1016/j.ces.2013.04.014.

Bayraktar, E., Mierka, O., Turek, S., 2012. Benchmark computations of 3D laminar flow around a cylinder with CFX, OpenFOAM and FeatFlow. Int. J. Comput. Sci. Eng., 7(3), 253-266, https://doi.org/10.1504/IJCSE.2012.048245.

Bobers, J., Grühn, J., Höving, S., Pyka, T., Kockmann, N., 2020. Two-phase Flow in Coiled Flow Inverter – Process Development and Scale-out From Batch to Continuous Flow, Org. Proc. R&D, 24(10), 2094-2105, https://doi.org/10.1021/acs.oprd.0c00152.

Bolivar, J.M., Nidetzky, B., 2013. Multiphase biotransformations in microstructured reactors: Opportunities for biocatalytic process intensification and smart flow processing. Green Proc. & Synth. 2(6), 541-559, https://doi.org/10.1515/gps-2013-0091.

Chatterjee, S., Ghanta, K.Ch., Hens, A., 2021. Study of multiphase flow inside straight and spiral microchannel and effect of two phase flow on Dean's vortices, Chem. Eng. Res. Des. 165, 398-408, https://doi.org/10.1016/j.cherd.2020.11.022.

Damanik, H.; Hron, J.; Ouazzi, A.; Turek, S., 2010. A monolithic FEM approach for the log-conformation reformulation (LCR) of viscoelastic flow problems, J. Non-Newtonian Fluid Mech., 19-20, 165, 1105-1113, doi:10.1016/j.jnnfm2010.05.008.

Dani, A., Guiraud, P., Cockx, A., 2007. Local measurement of oxygen transfer around a single bubble by planar laser-induced fluorescence. Chem. Eng. Sci., 62(24), 7245-7252, https://doi.org/10.1016/j.ces.2007.08.047.

Day, P., Manz, A., Zhang, Y., 2012. Microdroplet Technology: Principles and Emerging Applications in Biology and Chemistry. Springer, New York, NY, https://doi.org/10.1007/978-1-4614-3265-4.

Dean, W.R., 1928. Fluid motion in a curved channel, Proc. Royal Soc. A: Math. Phys. Eng. Sci., 121(787), 402-420, https://doi.org/10.1098/rspa.1928.0205.

Dittmar, I., Ehrhard, P., 2011. Numerical study of liquid/liquid slug flow in a capillary microreactor. Proc. Appl. Math. Mech., 11(1), 617-618, https://doi.org/10.1002/pamm.201110298.

Gaddem, M.R., Ookawara, S., Nigam, K.D.P., Yoshikawa, S., Matsumoto, H., 2021. Numerical modeling of segmented flow in coiled flow inverter: Hydrodynamics and mass transfer studies, Chem. Eng. Sci. 234, 116400, https://doi.org/10.1016/j.ces.2020.116400.

Gelhausen, M.G., Kurt, S.K., Kockmann, N., 2014. Mixing and heat transfer in helical capillary flow reactors with alternating bends. In ASME Int. Conf. Nano, Micro, and Minichannels, Vol. 46278, V001T13A001.

Grühn, J., Behr, A.S., Rosenthal, K., Kockmann, N., 2022. From coiled flow inverter to stirred tank reactor - Bioprocess development and ontology design, Chem. Ing. Technik, 94 (6), 852-863, doi.org/10.1002/cite.202100177.

Gutiérrez, E., Balcázar, N., Bartrons, E., Rigola, J., 2017. Numerical study of Taylor bubbles rising in a stagnant liquid using a level-set/moving-mesh method. Chemical Engineering Science, 164, 158-177. DOI: 10.1016/j.ces.2017.02.018.

Hessel, V., Loewe, H., Schoenfeld, F., 2005. Micromixers - a review on passive and active mixing principles. Chem. Eng. Sci., 60(8-9), 2479–2501.

Hessel, V., Kralisch, D., Kockmann, N., 2015. Novel Process Windows. Wiley-VCH, Weinheim, 2015, https://doi.org/10.1002/9783527654826.

Hron, J., Turek, S., 2006. A Monolithic FEM/Multigrid Solver for an ALE Formulation of Fluid-Structure Interaction with Applications in Biomechanics. In: Bungartz, HJ., Schäfer, M. (eds) Fluid-Structure Interaction. Lecture Notes in Computational Science and Engineering, vol 53. Springer, Berlin, Heidelberg. https://doi.org/10.1007/3-540-34596-5_7.

Hysing, S., 2007. Numerical Simulation of Immiscible Fluids with FEM Level Set Techniques. Dissertation, TU Dortmund University, Dortmund.

Hysing, S., Turek, S., Kuzmin, D., Parolini, N., Burman, E., Ganesan, S., Tobiska, L., 2009. Quantitative benchmark computations of two-dimensional bubble dynamics, Int. J. Numer. Methods Fluids, 60(11), 1259-1288, https://doi.org/10.1002/fld.1934.

Kashid, M.N., Agar, D.W., Turek, S., 2007a. CFD modelling of mass transfer with and without chemical reaction in the liquid/liquid slug flow microreactor, Chem. Eng. Sci. 62, 18-20, 5102-5109, https://doi.org/10.1016/j.ces.2007.01.068.

Kashid, M.N., Harshe, Y.M., Agar, D.W., 2007b. Liquid-liquid slug flow in a capillary: An alternative to suspended drop or film contactors. Ind. Eng. Chem. Res., 46(25), 8420–8430.

Kashid, M.N., Renken, A., Kiwi-Minsker, L., 2011. Gas–liquid and liquid–liquid mass transfer in microstructured reactors. Chem. Eng. Sci., 66(17), 3876–3897, https://doi.org/10.1016/j.ces.2011.05.015.

Klutz, S., Kurt, S.K., Lobedann, M., Kockmann, N., 2015. Narrow residence time distribution in tubular reactor concept for Reynolds number range of 10–100. Chem. Eng. R&D, 95, 22–33. https://dx.doi.org/10.1016%2Fj.cherd.2015.01.003.

Kockmann, N., 2006, Micro Process Engineering. Wiley-VCH, Weinheim, 2006, https://doi.org/10.1002/9783527616749.

Kockmann, N., Kiefer, T., Engler, M., Woias, P., 2006. Convective Mixing and Chemical Reactions in Microchannels with High Flow Rates, Sens. & Act. B 117, 495-508, https://doi.org/10.1016/j.snb.2006.01.004

Kockmann, N., Gottsponer, M., Roberge, D.M., 2011. Scale-up concept of single-channel microreactors from process development to industrial production. Chem. Eng. J., 167(2-3), 718–726, https://doi.org/10.1016/j.cej.2010.08.089.

Krieger, W., Lamsfuß, J., Zhang, W., Kockmann, N., 2017. Local Mass Transfer Phenomena and Chemical Selectivity of Gas-Liquid Reactions in Capillaries, Chem. Eng. & Technol., 40(11) 2134-2143, https://doi.org/10.1002/ceat.201700420.

Kumar, V., Aggarwal, M., Nigam, K.D.P., 2006. Mixing in curved tubes. Chem. Eng. Sci., 61(17), 5742–5753. https://doi.org/10.1016/j.ces.2006.04.040.

Kurt, S.K., Warnebold, F., Nigam, K.D., Kockmann, N., 2017. Gas-liquid reaction and mass transfer in microstructured coiled flow inverter. Chem. Eng. Sci., 169, 164-178, https://doi.org/10.1016/j.ces.2017.01.017.

Liu, Y., Ozbayoglu, E. M., Upchurch, E. R., Baldino, S., 2023. Computational fluid dynamics simulations of Taylor bubbles rising in vertical and inclined concentric annuli. International Journal of Multiphase Flow, 159, 104333. DOI: 10.1016/j.ijmultiphaseflow.2022.104333.

Lizarraga-Garcia, E., Buongiorno, J., Al-Safran, E., 2017. A broadly-applicable unified closure relation for Taylor bubble rise velocity in pipes with stagnant liquid. International Journal of Multiphase Flow, 89, 345-358. DOI: 10.1016/j.ijmultiphaseflow.2016.11.001.

Lizarraga-Garcia, E., Buongiorno, J., Al-Safran, E., 2021. Computational Fluid Dynamics (CFD) Simulations of Taylor Bubbles in Vertical and Inclined Pipes with Upward and Downward Liquid Flow. SPE Journal, 26(06), 3832-3847. DOI: 10.2118/205373-PA.

López-Guajardo, E., Ortiz-Nadal, E., Montesinos-Castellanos, A. Nigam, K.D.P., 2017. Coiled flow inverter as a novel alternative for the intensification of a liquid-liquid reaction. Chem. Eng. Sci., 169, 179-185, https://doi.org/10.1016/j.ces.2017.01.016.

Marschall, H., Boden, S., Lehrenfeld, C., Falconi D., C. J., Hampel, U., Reusken, A., Wörner, M., Bothe, D., 2014. Validation of Interface Capturing and Tracking techniques with different surface tension treatments against a Taylor bubble benchmark problem. Computers & Fluids, 102, 336-352. DOI: 10.1016/j.compfluid.2014.06.030.

Massoud, E.Z., Xiao, Q., El-Gamal, H.A., Teamah, M.A., 2018. Numerical study of an individual Taylor bubble rising through stagnant liquids under laminar flow regime. Ocean Engineering, 162, 117-137. DOI: 10.1016/j.oceaneng.2018.04.096.

Mierka, O., Turek, S., 2021. Numerical Simulation Techniques for the Efficient and Accurate Treatment of Local Fluidic Transport Processes Together with Chemical Reactions. In: Schlüter, M., Bothe, D., Herres-Pawlis, S., Nieken, U. (Eds.), Reactive Bubbly Flows. Fluid Mechanics and Its Applications, Springer Cham, https://doi.org/10.1007/978-3-030-72361-3_17.

Miessner, U., Helmers, T., Lindken, R., Westerweel, J., 2020. µPIV Measurement of the 3D velocity distribution of Taylor droplets moving in a square horizontal channel. Exp. Fluids, 61, 125, https://doi.org/10.1007/s00348-020-02949-z.

Müller, C., Kováts, P. and Zähringer, K., 2021. Experimental characterization of mixing and flow field in the liquid plugs of gas–liquid flow in a helically coiled reactor. Experiments in Fluids, 62(9), 190, https://doi.org/10.1007/s00348-021-03284-7.

Rojahn, P., Hessel, V., Nigam, K.D.P., Schael, F., 2018. Applicability of the axial dispersion model to coiled flow inverters containing single liquid phase and segmented liquid-liquid flows. Chem. Eng. Sci., 182, 77–92. https://doi.org/10.1016/j.ces.2018.02.031.

Roudet, M., Loubiere, K., Gourdon, C., Cabassud, M., 2011. Hydrodynamic and mass transfer in inertial gas–liquid flow regimes through straight and meandering millimetric square channels, Chem. Eng. Sci., 66, 2974–2990, https://doi.org/10.1016/j.ces.2011.03.045.

Saxena, A.K., Nigam K.D.P., 1984. Coiled configuration for flow inversion and its effect on residence time distribution, AIChE J. 30, 363–368, https://doi.org/10.1002/aic.690300303.

Schlüter, M., Kexel, F., von Kameke, A., Hoffmann, M., Herres-Pawlis, S., Klüfers, P., Oßberger, M., Turek, S., Mierka, O., Kockmann, N., Krieger, W., 2021. Visualization and Quantitative Analysis of Consecutive Reactions in Taylor Bubble Flows, pp 507-543 in: Schlüter, M., Herres-Pawlis, S., Nieken,, U., (Eds.) Reactive Bubbly Flows. Fluid Mechanics and Its Applications, vol 128. Springer, Cham, 2021, doi.org/10.1007/978-3-030-72361-3_21.

Shao, N., Gavriilidis, A., Angeli, P., 2009. Flow regimes for adiabatic gas–liquid flow in microchannels. Chemical Engineering Science, 64(11), 2749–2761, https://doi.org/10.1016/j.ces.2009.01.067.

Sobieszuk, P., Aubin, J., Pohorecki, R., 2012. Hydrodynamics and mass transfer in gas-liquid flows in microreactors. Chem. Eng. & Technol., 35(8), 1346–1358, https://doi.org/10.1002/ceat.201100643.

Srinivasan, R., Natarajan, S., 2012. Developments in inherent safety: A review of the progress during 2001–2011 and opportunities ahead. Process Saf. Environ. Prot., 90(5), 389-403, https://doi.org/10.1016/j.psep.2012.06.001.

Sudarsan, A.P., Ugaz, V.M., 2006. Multivortex micromixing. Proc. Nat. Acad. Sci., 103(19), 7228–7233. https://doi.org/10.1073/pnas.0507976103.

Taitel, Y., Bornea, D., Dukler, A.E., 1980. Modelling flow pattern transitions for steady upward gas-liquid flow in vertical tubes. AIChE J., 26(3), 345–354, https://doi.org/10.1002/aic.690260304.

Taylor, G.I., 1961. Deposition of a viscous fluid on the wall of a tube. J. Fluid Mech., 10(02), 161.

Turek, S., 1997. On discrete projection methods for the incompressible Navier-Stokes equations: an algorithmical approach. Comput. Methods Appl. Mech. Eng. 143(3-4), 271-288, https://doi.org/10.1016/S0045-7825(96)01155-3.

Turek, S., Mierka, O., Bäumler, K., 2019. Numerical Benchmarking for 3D Multiphase Flow: New Results for a Rising Bubble. In Numerical Mathematics and Advanced Applications (pp. 593-601). Springer. https://doi.org/10.1007/978-3-319-96415-7_54.

Vashisth, S., Nigam, K.D.P., 2008. Liquid-phase residence time distribution for two-phase flow in coiled flow inverter. Ind. & Eng. Chem. Res., 47(10), 3630–3638.

Waelchli, S., von Rohr, P.R., 2006. Two-phase flow characteristics in gas–liquid microreactors. Intl. J. Multiphase Flow, 32(7), 791–806, https://doi.org/10.1016/j.ijmultiphaseflow.2006.02.014.

Wörner, M., 2012. Numerical modeling of multiphase flows in microfluidics and micro process engineering: a review of methods and applications. Microfl. Nanofl. 12, 841-886, https://doi.org/10.1007/s10404-012-0940-8.

Yang L., Nieves-Remacha M.J., Jensen K.F., 2017. Simulations and analysis of multiphase transport and reaction in segmented flow microreactors, Chem. Eng. Sci. 169, 106-116, https://doi.org/10.1016/j.ces.2016.12.003.

Zhang, X., Stefanick, S., Villani, F.J., 2004. Application of microreactor technology in process development. Org. Proc. R&D, 8, 455-460, https://doi.org/10.1021/op034193x.